Calhoun: The NPS Institutional Archive

DSpace Repository

Theses and Dissertations | 1. Thesis and Dissertation Collection, all items

2006-06

Modeling fluid flow by exploring different flow geometries and effect of weak compressibility

Sopko, James J.

Monterey, California. Naval Postgraduate School

http://hdl.handle.net/10945/2713

This publication is a work of the U.S. Government as defined in Title 17, United States Code, Section 101. Copyright protection is not available for this work in the United States.

Downloaded from NPS Archive: Calhoun

http://www.nps.edu/library

Calhoun is the Naval Postgraduate School's public access digital repository for research materials and institutional publications created by the NPS community. Calhoun is named for Professor of Mathematics Guy K. Calhoun, NPS's first appointed -- and published -- scholarly author.

Dudley Knox Library / Naval Postgraduate School
411 Dyer Road / 1 University Circle
Monterey, California USA 93943

NAVAL POSTGRADUATE SCHOOL

MONTEREY, CALIFORNIA

THESIS

MODELING FLUID FLOW BY EXPLORING DIFFERENT FLOW GEOMETRIES AND EFFECT OF WEAK COMPRESSIBILITY

by

James J. Sopko

June 2006

Thesis Advisor:	Hong Zhou
Second Reader:	Clyde Scandrett

Approved for public release, distribution is unlimited

THIS PAGE INTENTIONALLY LEFT BLANK

REPORT DOCUMENTATION PAGE			Form Approved OMB No. 0704-0188

Public reporting burden for this collection of information is estimated to average 1 hour per response, including the time for reviewing instruction, searching existing data sources, gathering and maintaining the data needed, and completing and reviewing the collection of information. Send comments regarding this burden estimate or any other aspect of this collection of information, including suggestions for reducing this burden, to Washington headquarters Services, Directorate for Information Operations and Reports, 1215 Jefferson Davis Highway, Suite 1204, Arlington, VA 22202-4302, and to the Office of Management and Budget, Paperwork Reduction Project (0704-0188) Washington DC 20503.

1. AGENCY USE ONLY *(Leave blank)*	2. REPORT DATE June 2006	3. REPORT TYPE AND DATES COVERED Master's Thesis

4. TITLE AND SUBTITLE Modeling Fluid Flow by Exploring Different Flow Geometries and Effect of Weak Compressibility.	5. FUNDING NUMBERS
6. AUTHOR James J. Sopko	
7. PERFORMING ORGANIZATION NAME AND ADDRESS Naval Postgraduate School Monterey, CA 93943-5000	8. PERFORMING ORGANIZATION REPORT NUMBER
9. SPONSORING /MONITORING AGENCY NAME(S) AND ADDRESS(ES) N/A	10. SPONSORING/MONITORING AGENCY REPORT NUMBER

11. SUPPLEMENTARY NOTES The views expressed in this thesis are those of the author and do not reflect the official policy or position of the Department of Defense or the U.S. Government.

12a. DISTRIBUTION / AVAILABILITY STATEMENT Approved for public release, distribution is unlimited	12b. DISTRIBUTION CODE

13. ABSTRACT (maximum 200 words) Atmospheric mixing is a problem of exceptional importance and difficult to study. The anelastic approximation is the accepted fluid system governing the atmosphere over large vertical scales (about 8 km). The anelastic equations, unlike the Navier-Stokes equations, incorporate a nontrivial spatial divergence constraint on the velocity field. This yields a weakly compressible fluid flow. The basis of this study is to use numerical analysis to explore the effects of weak compressibility in the evolution of fluid governed by the anelastic equations, and the effects of incompressibility governed by the Navier-Stokes equation. The analysis then goes on to investigate the difference between three different initial conditions. Within each initial condition different density profiles are observed while varying parameters are investigated. Numerical results show that comparisons of incompressible Navier-Stokes equations to the anelastic fluid flow equations do not produce similar results. The weakly compressible flow creates a mixing barrier, stopping vertical fluid exchange. The perturbed middle region initial condition creates a chaotic environment that prevents vortices from merging.

14. SUBJECT TERMS Navier-Stokes equation, anelastic equations, numerical analysis, incompressible flow, weakly compressible flow, undersea warfare	15. NUMBER OF PAGES 71
	16. PRICE CODE

17. SECURITY CLASSIFICATION OF REPORT	18. SECURITY CLASSIFICATION OF THIS PAGE	19. SECURITY CLASSIFICATION OF ABSTRACT	20. LIMITATION OF ABSTRACT
Unclassified	Unclassified	Unclassified	UL

NSN 7540-01-280-5500 Standard Form 298 (Rev. 2-89)
Prescribed by ANSI Std. 239-18

THIS PAGE INTENTIONALLY LEFT BLANK

Approved for public release, distribution is unlimited

MODELING FLUID FLOW BY EXPLORING DIFFERENT FLOW GEOMETRIES AND EFFECT OF WEAK COMPRESSIBILITY

James J. Sopko
Ensign, United States Navy
B.S., United States Naval Academy, 2005

Submitted in partial fulfillment of the
requirements for the degree of

MASTER OF SCIENCE IN APPLIED MATHEMATICS

from the

NAVAL POSTGRADUATE SCHOOL
June 2006

Author: James J. Sopko

Approved by: Dr. Hong Zhou
Thesis Advisor

Dr. Clyde Scandrett
Second Reader

Dr. Clyde Scandrett
Chairman, Department of Applied Mathematics

THIS PAGE INTENTIONALLY LEFT BLANK

ABSTRACT

Atmospheric mixing is a problem of exceptional importance and difficult to study. The anelastic approximation is the accepted fluid system governing the atmosphere over large vertical scales (about 8 km). The anelastic equations, unlike the Navier-Stokes equations, incorporate a nontrivial spatial divergence constraint on the velocity field. This yields a weakly compressible fluid flow. The basis of this study is to use numerical analysis to explore the effects of weak compressibility in the evolution of fluid governed by the anelastic equations, and the effects of incompressibility governed by the Navier-Stokes equation. The analysis then goes on to investigate the difference between three different initial conditions. Within each initial condition different density profiles are observed while varying parameters are investigated. Numerical results show that comparisons of incompressible Navier-Stokes equations to the anelastic fluid flow equations do not produce similar results. The weakly compressible flow creates a mixing barrier, stopping vertical fluid exchange. The perturbed middle region initial condition creates a chaotic environment that prevents vortices from merging.

THIS PAGE INTENTIONALLY LEFT BLANK

TABLE OF CONTENTS

I. INTRODUCTION 1

II. NUMERICAL METHODS 15
- A. INTRODUCTION TO THE PROBLEM 15
- B. PROJECTION METHOD FOR NAVIER-STOKES EQUATIONS 16
- C. SOLVING POISSON'S EQUATION IN A SEMI-PERIODIC REGION 20
- D. NUMERICAL METHODS FOR THE WEAKLY COMPRESSIBLE MODEL 23
- E. TIME STEP CONTROL AND BOUNDARY CONDITIONS 26

III. NUMERICAL RESULTS 31
- A. INCOMPRESSIBLE MODEL 34
  - 1. Stream Function Initial Condition 34
  - 2. Perturbed Middle Region Initial Condition 36
  - 3. Poiseuille Flow Initial Condition 37
- B. WEAKLY COMPRESSIBLE MODEL 38
  - 1. Stream Function Initial Condition 38
    - *a. Exponential Density Profile 38*
    - *b. Hyperbolic Tangent Density Profile 41*
    - *c. Linear Density Profile 42*
  - 2. Perturbed Middle Region Initial Condition 43
    - *a. Exponential Density Profile 43*
    - *b. Hyperbolic Tangent Density Profile 46*
    - *c. Linear Density Profile 47*
  - 3. Poiseuille Flow Initial Condition 48

IV. CONCLUSIONS 49

LIST OF REFERENCES 53

BIBLIOGRAPHY 55

INITIAL DISTRIBUTION LIST 57

THIS PAGE INTENTIONALLY LEFT BLANK

LIST OF FIGURES

Figure 1. Diagram of the Flow Region with No-Slip Vertical Boundary Conditions and Periodic Horizontal Boundary Conditions.....7
Figure 2. Exponential density profile with three different values for α.....11
Figure 3. Hyperbolic tangent density profile.....11
Figure 4. Linear Density Profile.....12
Figure 5. Standard cellular flow initial condition shown in colored vortex scheme and vector field.....32
Figure 6. Perturbed middle region initial condition in colored vortex scheme and vector field.....33
Figure 7. Poiseuille flow initial condition in colored vortex scheme and vector field.....33
Figure 8. Incompressible model with a standard cellular flow initial condition.....35
Figure 9. Results of perturbed middle region initial condition with Navier-Stokes equation.....36
Figure 10. Poiseuille flow initial condition computed with incompressible Navier-Stokes equations and a colorbar showing magnitude of velocity.....37
Figure 11. Results for cellular flow initial condition with an exponential density profile and $\alpha = .02$. .38
Figure 12. Results for cellular flow initial condition with an exponential density profile and $\alpha = .05$. .40
Figure 13. Results for standard cellular flow initial condition with an exponential density profile and $\alpha = .1$. 41
Figure 14. Weakly compressible system with standard cellular flow and hyperbolic tangent density profile.....42
Figure 15. Results of standard cellular flow initial condition with a linear density profile.....43
Figure 16. Numerical Results for perturbed middle region initial condition with $\alpha = .02$ in the exponential density profile.....44
Figure 17. Numerical results for perturbed middle region initial conditions and a exponential density profile with $\alpha = .05$. 45
Figure 18. Numerical results for perturbed middle region initial conditions and an exponential density profile with $\alpha = .1$. 46

Figure 19. Numerical results for perturbed middle region initial condition with a hyperbolic tangent density profile.....47
Figure 20. Numerical results for perturbed middle region initial condition and a linear density profile..48

ACKNOWLEDGEMENTS

I would like to thank Dr. Hong Zhou for her constant guidance on this study. Her notes and endless knowledge were crucial for the development of this thesis.

Dr. Clyde Scandrett, Chair of the Applied Mathematics Department at NPS, also deserves my sincere thanks. His contributions to understanding of material and editing can not go unmentioned.

I would also like to thank Dr. Anne Almgren for private communications and for sharing her personal notes with me.

THIS PAGE INTENTIONALLY LEFT BLANK

I. INTRODUCTION

Understanding the mixing properties of fluids in the atmosphere is not simple and accurately representing and understanding these properties in a model can present a lifetime of work. It is understood that the mixing of fluids is limited by the governing principles of physics. To begin to comprehend, one must compare different models and determine what factors drive the geometric flows produced. However, models are unable to perfectly represent what occurs in nature. To make a mathematical model tractable, we must often make assumptions to simplify the analysis.

$$\rho(z)\frac{D\vec{u}}{Dt} = -\nabla p + \mu\Delta\vec{u} - \rho(z)g\cdot\hat{k} \tag{1}$$

$$\frac{\partial\rho(z)}{\partial t} + \nabla\cdot(\rho(z)\vec{u}) = 0 \tag{2}$$

Equations (1) and (2) were the first set of equations used to model fully compressible atmospheric fluid flow. In these equations $\frac{D}{Dt} = \frac{\partial}{\partial t} + \vec{u}\cdot\nabla$, is an operator often referred to as the material derivative; $\rho(z)$ is the density profile as a function of altitude; $\vec{u}$ is the directional fluid velocity; μ is viscosity; p is the pressure; $\Delta\vec{u}$ is the Laplacian of $\vec{u}$; and g is gravity. Equation (1) represents the momentum equation and equation (2) is the conservation of mass equation for fluid flow.[1]

[1] G. K. Batchelor, *An Introduction to Fluid Dynamics*, (New York: Cambridge University Press, 1967): xviii, 74, 166.

Note that equations (1) and (2) are not scaled; meaning each variable and constant is associated with a metric unit.

We now introduce the Reynolds number, Re. It is a non-dimensional value used for viscosity. The Reynolds number is one of the key non-dimensional coefficients in the study. It is ratio of inertial forces to viscous forces which is non-dimensional and is on the scale of 10^3.

Now we can begin to show how these equations can be reduced to the anelastic equations that will be used in this study.

The Boussinesq equations, (3) are a common approximation for the conservation of mass equation used to model fluids in the atmosphere.

$$\bar{u}_t + (\bar{u} \cdot \nabla)\bar{u} = -\frac{1}{\rho}\nabla p + \frac{1}{Re \cdot \rho}\Delta \bar{u} - \bar{g} \cdot \hat{k} \tag{3}$$

$$\nabla \cdot \bar{u} = 0 \tag{4}$$

These equations are the momentum equation, (3) and conservation of mass equation, (4), but are now scaled, or non-dimensionalized.

Problems in the analysis of the Boussinesq equations are that they are invalid over large vertical scales and that numerical methods become more complex and less efficient. This has led to many studies attempting to simplify the Boussinesq equations. One such simplification evolved into the anelastic equations.

The anelastic equations have been derived into several different forms for use in modeling small scale atmospheric

flow. A primary reason the anelastic equations are used instead of the full Navier-Stokes equations is because of numerical stability requirements for time-stepping when compressibility of the fluid is allowed and a CFL condition is based upon the sound speed of the fluid rather than its large scale flow velocities. In fact, the term anelastic is referred to as "sound proof."

Batchelor (1953) derived an approximation to the conservation of mass equation, rewritten below. This is equivalent to equation (2),

$$\nabla \cdot \bar{\mathrm{u}} = -\frac{1}{\rho(z)} \frac{D\rho(z)}{Dt} \tag{5}$$

assuming a dry ideal gas atmosphere with small pressure deviations from an adiabatic reference state. The time scale, τ, equals $\frac{L}{U}$, where L is a representative length, or altitude, U is a characteristic fluid velocity of the medium. Durran, in his paper on the anelastic approximation, assumes that $\left|\frac{p-p_a}{p_a}\right| \ll 1$, implying that the deviation of pressure from the reference state pressure (adiabatic) is very small.[2] This small pressure deviation from the reference state pressure directly relates to a small Mach number, which is the ratio of fluid velocity to the speed of sound in the medium.

Although not his primary goal, he managed to achieve a set of equations that effectively filtered sound waves, (6) ; where v is the vertical component of $\bar{\mathrm{u}}$, γ is the ratio of specific heat at constant pressure to specific heat at

[2] G. K. Batchelor, "The Conditions for Dynamical Similarity of Motions of a Frictionless Perfect-Gas Atmosphere," *Quart. J. R. Meteor. Soc.* 79 (1953): 229.

constant volume ($\gamma = \frac{c_p}{c_v}$), p_a is the pressure at adiabatic equilibrium, and $\rho_a(z)$ is the density at the adiabatic equilibrium.[3]

$$\nabla \cdot \vec{u} = \frac{vg\rho_a(z)}{\gamma p_a} \tag{6}$$

Ogura & Phillips (1962) then derived the same equation as Batchelor (1953). However, they presented a more rigorous scaling analysis using a different set of assumptions. They introduced an almost constant non-dimensional potential temperature, and a time scale based upon the Brunt-Väisälä frequency. Their first assumption is that $\frac{\delta\theta}{\Theta} \ll 1$, where $\delta\theta$ is the deviation of the potential temperature from an adiabatic reference state potential temperature, Θ. The second assumption involves neglecting small amplitude, high frequency fluid oscillations in a resting isothermal atmosphere.

> This theory shows that two types of wave motion can exist under these [adiabatic] circumstances, acoustic waves and gravity waves. The acoustic waves in general have high frequencies, while the gravity waves have low frequencies.[4]

The frequency separating the two wave motions is known as the Brunt-Väisälä frequency, N, $N^2 = g \cdot \frac{\partial \ln\theta'}{\partial z'}$. Due to their focus of analyzing the influence of gravity waves, Ogura & Phillips' (1962) assumption stated the time scale τ is bounded from below by the inverse of the Brunt-Väisälä frequency, N^{-1}.

---

[3] G.K. Batchelor, "The Conditions for Dynamical Similarity of Motions of a Frictionless Perfect-Gas Atmosphere," *Q. J. R. Meteorol. Soc.* 79 (1953): 225-30.

[4] Y. Ogura and N. A. Phillips, "Scale Analysis of Deep and Shallow Convection in the Atmosphere," *J. Atmos. Sci.* 19, no. 2 (1962): 174.

Batchelor (1953) and Ogura & Phillips (1962) only considered a dry adiabatic atmosphere in their derivations. More work has been done since to apply the anelastic equations to moist atmospheres. Gough (1969) assumes relative density and temperature variations in the atmosphere are small. He defines the length scale to be the minimum of the depth of the atmospheric layer where motion occurs and the mean pressure scale height. His time scale assumption relates to frequency also. He then assumes the time scale is no shorter than the time it takes for a characteristic vertical velocity to traverse the length scale. These and other scalings lead to the upper bound of the Mach number squared to be defined as the rough magnitudes of the density and temperature variations.[5]

Wilhelmson & Ogura (1972) transformed the governing equations so they would be useful with deep moist convection. Although other researchers have concluded that pressure perturbations must be small, they discovered that the pressure perturbation is an order of magnitude smaller than scale analysis indicates and therefore concluded it can be ignored.[6]

Lipps & Hemler (1982) require in their analysis that the non-isentropic base state potential temperature vary with z, altitude. Since this study does not consider temperature it has not been included in our analysis, but could be used in further studies is temperature were to be considered an important factor.

---

[5] D. O. Gough, "The Anelastic Approximation for Thermal Convection," *J. Atmos. Sci.* 26 (1969): 450-56.

[6] R. Wilhelmson and Y. Ogura, "The Pressure Perturbation and the Numerical Modeling of a Cloud," *J. Atmos. Sci.* 29 (1972): 1306

In 1989, Durran formulated the "pseudo-incompressible" anelastic equation by assuming small pressure deviations from a base state that avoids a CFL time-step stability requirement based upon the speed of sound in the medium.

The conservation of mass equation, used in this study, was first derived in 1984 when some researchers were looking to model the flow of cold heavy vapor following a liquefied natural gas (LNG) spill. They developed an equation where density variations are independent of time. We adopt this approach and so variations in density will therefore depend solely upon variations of the spatial coordinates of fluid elements.

To understand the mixing behavior, we focus our study on a simple model problem. The problem is defined by a non-dimensional channel flow with prescribed boundary conditions. The vertical fluid motion is limited by two parallel fixed boundaries separated by a distance Z_L. We assume no-slip boundary conditions on the channel walls and periodic boundary conditions over a horizontal width M. Figure 1 offers a visual of the model's structure.

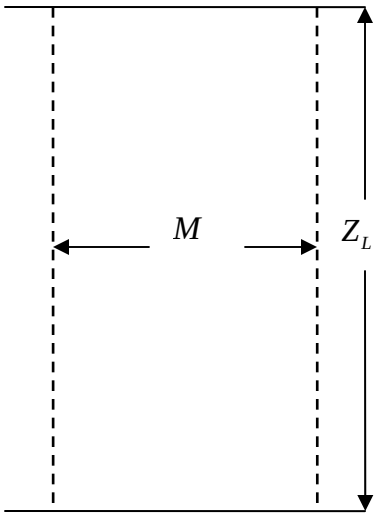

Figure 1. Diagram of the Flow Region with No-Slip Vertical Boundary Conditions and Periodic Horizontal Boundary Conditions.

Jarvis and McKenzie (1980) wrote that a strong density variation, given by some mean state $\rho(z)$, a function of altitude, must be consistently modeled.[7] In this study we are not going to use the Boussinesq equations common of previous studies concerning geometric flow because they are not valid over large vertical scales in which density is most likely to vary. Instead, we use an approximation of the Boussinesq equations known as the anelastic fluid equations. Use of the anelastic fluid equations in the study of atmospheric fluid flow has been justified in previous studies.[8,9,10,11] Bannon (1996) wrote,

[7] G. Jarvis and D. McKenzie, "Convection in a Compressible Fluid with Infinite Prandtl Number," *J. Fluid Mech.* 96, no. 13 (1980): 517-18.

[8] G. K. Batchelor, "The Conditions for Dynamical Similarity of Motions of a Frictionless Perfect-Gas Atmosphere," *Q. J. R. Meteorol. Soc.* 79 (1953): 224-35.

[9] D. R. Durran, "Improving the Anelastic Approximation," *J. Atmos. Sci.* 46 (1989): 1453.

[10] F. Lipps and R. Hemler, "A Scale Analysis of Deep Moist Convection and Some Related Numerical Calculations," *J. Atmos. Sci.* 39 (1982): 2192-2203.

> The anelastic approximation has been developed to remove the shortcoming of the Boussinesq approximation whose validity is limited to flows with a vertical scale much less than a density scale height.[12]

Another drawback with use of the Boussinesq equation is that updates of the fluid pressure require global inversions of elliptic operators.

Anelastic fluid flow equations allow us to model weakly compressible fluids as a compromise between fully compressible fluid flow (that require extremely small time steps) and the incompressible flow equation. This study will numerically solve the weakly compressible and incompressible fluid models and then compare different density profiles, initial conditions, and parameter changes within those models over a time frame comparable to what is required to achieve a steady state.

In our analysis we assume that the density is fixed in time and balanced by the hydrostatic pressure. The total pressure is assumed to vary only slightly from the hydrostatic pressure which is also independent of time. In other word we assume (7) and (8).

$$\rho_{\text{total}} = \rho(z) \tag{7}$$

$$p = p_a + p', \text{ when } \frac{p - p_a}{p_a} \ll 1 \tag{8}$$

The conservation of mass equation

[11] Y. Ogura and N. A. Phillips, "Scale Analysis of Deep and Shallow Convection in the Atmosphere," *J. Atmos. Sci.* 19, no. 2 (1962): 173-79.

[12] P. R. Bannon, "On the Anelastic Approximation for a Compressible Atmosphere," *J. Atmos. Sci.* 53, no. 23 (1996): 3618.

$$\frac{1}{\rho}\frac{D\rho}{Dt}+\nabla\cdot\vec{u}=0 \tag{9}$$

can also be written as

$$\frac{\partial\rho}{\partial t}+\nabla\cdot(\rho\vec{u})=0 \tag{10}$$

Now because ρ is only a function of z, we have $\frac{\partial\rho}{\partial t}=0$ and the anelastic equation governing conservation of mass is

$$\nabla\cdot(\rho(z)\vec{u})=0 \tag{11}$$

The anelastic equations are given in equations (12) and (13). The conservation of mass equation, (13), will distinguish between the anelastic equation and the incompressible equation formulations.

$$\vec{u}_t+(\vec{u}\cdot\nabla)\vec{u}=-\frac{1}{\rho(z)}\nabla p+\frac{1}{Re\rho(z)}\Delta\vec{u}-g \tag{12}$$

$$\nabla\cdot(\rho(z)\vec{u})=0 \tag{13}$$

All physical variables are non-dimensional to ease the use of numerical methods.[13] These equations model weakly compressible fluid flow for $\rho(z)\neq 1$, and from this point on in the paper will be referred to as the weakly compressible model. Incompressible fluids can be modeled by giving $\rho(z)$ a constant value of 1, leading to the incompressible continuity equation, (14).

$$\nabla\cdot\vec{u}=0 \tag{14}$$

The non-dimensionality of the equations allows for the omission of units in the numerical analysis. The Reynolds number in this study is roughly 1000 which is

[13] G. Jarvis and D. McKenzie, "Convection in a Compressible Fluid with Infinite Prandtl Number," *J. Fluid Mech.* 96, no. 13 (1980): 520

considered a low Reynolds number and yields laminar flow. A high Reynolds number, a value of around 4000, produces turbulent flow.

Like previous studies, pressure does not vary, but we do not consider temperature or density perturbations. Our goal is to look at the effect of different fixed density profiles under varying initial conditions, and parameters to compare the development of flow under the weakly compressible anelastic fluid model with that of the incompressible Navier-Stokes model.

Previous studies have claimed that solving the anelastic equations using methods of homogenized averaging show different effective mixing properties than those found using the completely incompressible flow equations[14,15]. McLaughlin, Zhou, and Forest (2003) demonstrated that deviations in the mean density profile of a fluid governed by anelastic equations yields new mixing phenomena.[16] We will show that further investigation of variations in the mean density profile likewise results in new types of flow, and that changing initial conditions yield various geometric flows and produce mixing barriers. Specifically we will consider the following density profiles:

[14] R. M. McLaughlin and M. G. Forest, "An Anelastic, Scale-Separated Model for Mixing, with Application to Atmospheric Transport Phenomena," ***Phys. Fluids*** 11, no 4 (1999): 880.

[15] R. M. McLaughlin, M. G. Forest, and H. Zhou, "Computational Study of Weakly Compressible Mixing Barrier in Low Prandtl Number, Strongly Stratified Fluids," ***Phys. Fluids*** 15, no 10 (2003): 2872-2885.

[16] R. M. McLaughlin, M. G. Forest, and H. Zhou, "Computational Study of Weakly Compressible Mixing Barrier in Low Prandtl Number, Strongly Stratified Fluids," ***Phys. Fluids*** 15, no 10 (2003): 2872-2885.

- $\rho^{-1}(z) = e^{\alpha z}$, where α is constant, but will be varied to create distinct density profiles and therefore results. This mean density profile represents an unstructured profile where the weight of the ideal gas compresses itself.

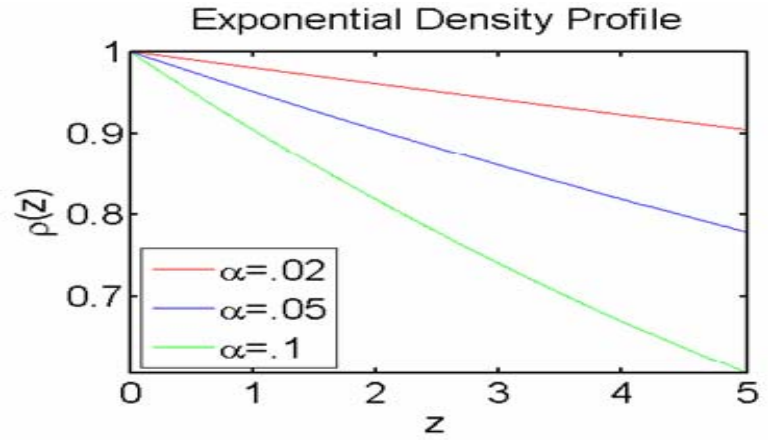

Figure 2. Exponential density profile with three different values for α.

- $\rho^{-1}(z) = 1 + \varepsilon \cdot \tanh[\delta(z - z_L/2)]$, where ε, δ, and z_L are constants. z_L is the width of the channel, ε sets the amplitude of the shift, and δ is the layer thickness. This profile represents a structured profile with a density transition layer. This profile is common at thermoclines in the ocean and boundary layers in the atmosphere.

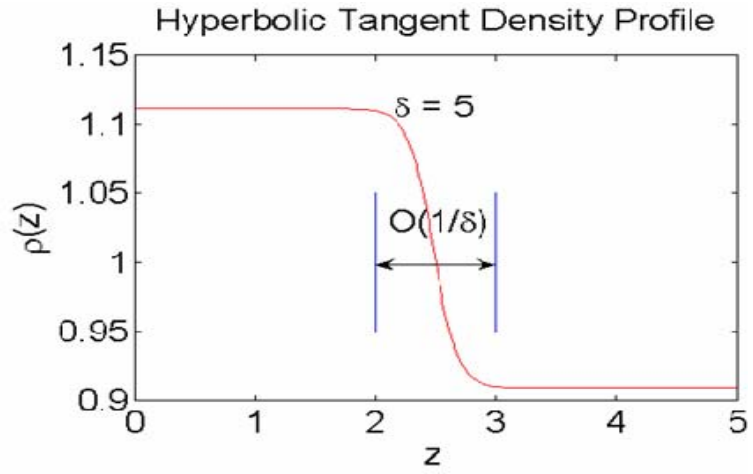

Figure 3. Hyperbolic tangent density profile.

- $\rho(z) = a \cdot z + 1.0$, where a is constant. a will serve as parameter, allowing us to see the affects of a linear density profile when $a \neq 0$, and a Navier-Stokes equation when $a = 0$. This study will research affects when $a = -0.02$.

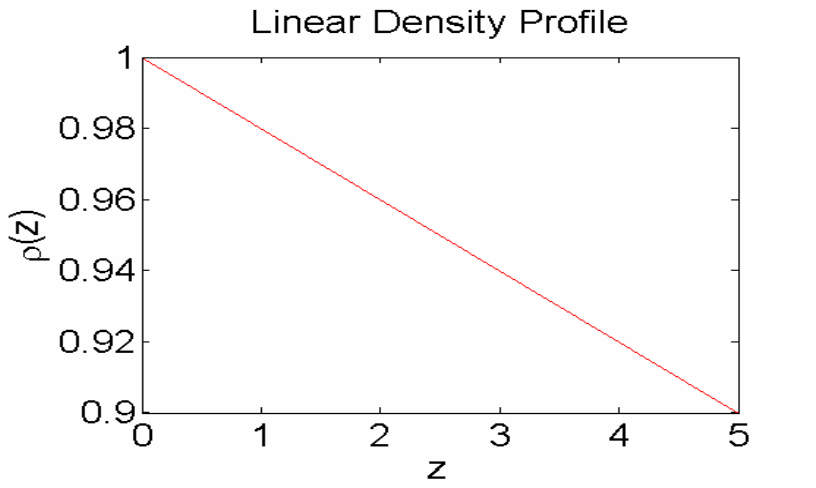

Figure 4. Linear Density Profile.

Here, ε, α, z_L and a are arbitrary constants that can be changed to observe the effects, and z is the independent variable signifying vertical distance within the layer, or altitude. None of the densities dealt with here allow for density perturbations. Of course, density perturbations are included in atmospheric flow, but for the purpose of this study, the effect of varying mean state density fields are considered rather than dynamic effects caused by buoyancy instabilities. For comparison, all density profiles can be manipulated to model incompressible Navier-Stokes results if $\rho(z) = 1$. Analysis of increasing the α term is conducted to show a breakdown of the numerical approaches as α increases for the exponential density profile.

Mathematically, our goal is to numerically solve a system of second order partial differential equations (PDE). To accomplish this feat, two numerical techniques

are used employing the finite difference method for spatial discretization and the predictor-corrector method for marching forward in time. The finite difference method utilizes a second order central difference approximation coupled with a divergence free constraint implemented by a projection method through the Hodge decomposition. The incompressible and weakly compressible models can be solved in a similar way by a simple change of variables. The detailed descriptions of the numerical methods are given in Chapter II, entitled Numerical Methods.

This research could act as a way of further understanding air currents and the factors that drive them. As meteorological affects and forecasting are important to the naval war fighter, this research may help in the understanding of the mathematics behind the meteorological models, and by performing sensitivity analysis, may lead to an increase in confidence of weather prediction

THIS PAGE INTENTIONALLY LEFT BLANK

II. NUMERICAL METHODS

A. INTRODUCTION TO THE PROBLEM

The fluid domain modeled is bounded on the top and bottom by two parallel fixed boundary conditions. These boundaries are separated by the vertical distance z_L while the sides of the numerical domain are separated by a horizontal distance, M.

As stated in the introduction the viscosity μ is constant. Therefore, the anelastic equations which govern the motion of the fluid are:

$$\vec{u}_t + (\vec{u}\cdot\nabla)\vec{u} = -\frac{1}{\rho(z)}\nabla P + \frac{1}{Re\rho(z)}\Delta\vec{u} - g\hat{k} \tag{15}$$

$$\nabla\cdot(\rho(z)\vec{u})=0 \tag{16}$$

$\rho(z)$ is the prescribed density as a function of altitude. This paper considers three density profiles detailed in the introduction: $\rho^{-1}(z) = e^{\alpha z}$, $\rho^{-1}(z) = 1+\varepsilon\cdot\tanh[\delta(z-z_L/2)]$, and . $\rho(z) = a\cdot z + 1.0$. In this study $a = .5$.

Let $\vec{u} = (u_1, u_2)$ be the fluid velocities in the x and z directions respectively. we make the simple change of dependent variable by incorporating the density variation into a new fluid momentum per unit volume, $\vec{v}$.

$$\begin{aligned} h(z) &= \tfrac{1}{\rho(z)}, \\ \vec{v} &= \rho(z)\vec{u} \end{aligned} \tag{17}$$

$\vec{v}=(\nu_1,\nu_2)^t$ is the new two-dimensional momentum per unit volume. Equations (15) and (16) become

$$\vec{v}_t + h(z)\vec{v}\cdot\nabla\vec{v} + h'(z)\begin{pmatrix} v_1 v_2 \\ v_2^2 \end{pmatrix} = -\nabla P + \frac{1}{Re}\Delta(h(z)\vec{v}) - \frac{g}{h(z)}\hat{k} \tag{18}$$

$$\nabla\cdot\vec{v}=0 \tag{19}$$

FORTRAN was the computer language used for this analysis. The original code originated from a study by McLaughlin, Zhou, and Forest.[17] However, some changes had to be made due to the evolution of the FORTRAN source code. Specifically, the compiler had to be updated from FORTRAN 66 to a newer FORTRAN 77. All codes were run on a LINUX machine to increase the speed of computations.

As stated in the introduction, numerical methods such as the finite difference method and predictor-corrector method are put to use on a cell-centered numerical grid system. The following sections describe the different methods applied to specific equations used to produce the numerical results.

B. PROJECTION METHOD FOR NAVIER-STOKES EQUATIONS

We use the projection method to solve the Navier-Stokes equation for incompressible fluids.[18] This projection method is based on the Hodge decomposition.[19] The Hodge decomposition is a splitting of an arbitrary vector field into two orthogonal components, one divergence free and the other the gradient scalar field. If $U^* = U^*(x)$ is a smooth vector field and $\vec{n}$ is a orthogonal unit vector

[17] R. M. McLaughlin, H. Zhou, M. G. Forest, "Computational Study of a Weakly Compressible Mixing Barrier in Low Prandtl Number, Strongly Stratified Fluids," ***Phys. Fluids*** 15, no. 10 (2003)

[18] A. J. Chorin, "Numerical Solution of Incompressible Flow Problems," ***Studies in Num. Anal.*** 2 (1997): 64-67

[19] A. J. Chorin and J. E. Marsden, ***A Mathematical Introduction to Fluid Mechanics***, New York: Springer-Verlag, 1990): 40.

defined on a smooth region D with $\int_{\partial D} U^* \cdot \vec{\mathrm{n}} dS = 0$, then U^* can be written as

$$U^* = U_d + \nabla\phi \tag{20}$$

where $\nabla \cdot U_d = 0$ (divergent free) and ϕ is the solution of the elliptic equation $\Delta\phi = \nabla \cdot U^*$ (Poisson's equation) in D, with $\frac{\partial\phi}{\partial n} = U^* \cdot \vec{\mathrm{n}}$ on ∂D. The decomposition is orthogonal with respect to the inner product, provided $U_d \cdot n = 0$ on the boundary of D, that is $\int U_d \cdot \nabla\phi dV = 0$. Note that in this numerical analysis $U_d = U^{n+1}$ and $\mathrm{P}(U^*)$ is the projection of U^* onto U_d using the Hodge decomposition of U^*. Now we give a detailed implementation of the projection method.

There are two steps used in the projection process for the Navier-Stokes equations. The first step involves a starting point, U^n, and finding an intermediate value for the velocity, U^*, from which we can project to find U^{n+1}.

$$\frac{U^* - U^n}{\Delta t} + \nabla\tilde{p}^{n-\frac{1}{2}} = -[(U \cdot \nabla)U]^{n+\frac{1}{2}} + \frac{1}{Re}\frac{\Delta(U^n + U^*)}{2} \tag{21}$$

$$U^{n+1} = \mathrm{P}(U^*) \tag{22}$$

We begin the time marching scheme with three known elements of equation (21): U^{n-1}, U^n, and $\nabla\tilde{p}^{n-\frac{1}{2}}$, at time $t = 0$ ($n = 0$). The quantity $[(U \cdot \nabla)U]^{n+\frac{1}{2}}$, known as the convection term, can be approximated by a second order finite difference extrapolation[20]:

[20] A. J. Chorin and J. E. Marsden, ***A Mathematical Introduction to Fluid Mechanics***, New York: Springer-Verlag, 1990): 40.

$$[(U\cdot\nabla)U]^{n+\frac{1}{2}} \approx \frac{1}{2}(3H^n - H^{n-1}) \tag{23}$$

where

$$H^n = [(U\cdot\nabla)U]^n \tag{24}$$

Center difference approximations are applied for approximating the Laplacian term and equation (21) is solved for the unknown intermediate velocity U^*

Equation (22) displays the projection operator, P applied to U^* to obtain U^{n+1}. This is the second step in the algorithm that as an intermediate step requires the solution of equation (25). In this equation, D is a discrete divergence operator and ϕ is the potential function of equation (20) needed to determine U^{n+1}.

$$\Delta\phi = DU^* \tag{25}$$

Equation (25) is an elliptic equation and in order to solve it numerically we use a fast Fourier transform (FFT) with periodic boundary conditions for ϕ in the horizontal direction and Neumann boundary conditions at the walls barricading the region from top and bottom. The numerical method for solving this Poisson's equation is discussed in Section C, entitled Solving Poisson's equation in a Semi-Periodic Region.

Equation (26) constitutes the projection of U^* onto it divergence free component, where ∇ is the gradient operator, and is used to solve for U^{n+1}.

$$U^{n+1} = U^* - \nabla\phi \tag{26}$$

The next step in the numerical algorithm is to update the pressure gradient using equation (27).

$$\nabla p^{n+\frac{1}{2}} = \nabla \tilde{p}^{n-\frac{1}{2}} + \frac{1}{\Delta t}(I - \mathrm{P})(U^*) = \nabla \tilde{p}^{n-\frac{1}{2}} + \frac{1}{\Delta t}\nabla \phi \tag{27}$$

As in equation (21), equation (27) has the $\nabla \tilde{p}^{n-\frac{1}{2}}$ term that is determined by using the same projection operator P used in equation (22).

$$\nabla \tilde{p}^{n-\frac{1}{2}} = (I - \mathrm{P})Q \tag{28}$$

where P is the projection operator and Q is represented by equation (29).

$$Q = U^n + \Delta t\left(-[(U \cdot \nabla)U]^{n+\frac{1}{2}} - \nabla p^{n-\frac{1}{2}} + \frac{1}{Re}\Delta U^n \right) \tag{29}$$

Initially, only the velocity field U^0 need be known. To initiate the algorithm, the following must first be solved

$$(I - \mathrm{P})\left(-[(U \cdot \nabla)U^0 + \frac{1}{Re}\Delta U^0 \right) = \nabla p^0 \tag{30}$$

to find ∇p^0. Once ∇p^0 is found, Euler's method can be used to find U^1 by solving a variant of equation (21).

$$\frac{U^1 - U^0}{\Delta t} + \nabla p^0 = -[(U \cdot \nabla)U]^0 + \frac{1}{Re}\Delta U^0 \tag{31}$$

Once U^1 is known, ∇p^1 is found by computing

$$(I - \mathrm{P})\left(-[(U \cdot \nabla)U]^1 + \frac{1}{Re}\Delta U^1 \right) = \nabla p^1 \tag{32}$$

and the average of ∇p^0 and ∇p^1 yields $\nabla p^{\frac{1}{2}}$:

$$\nabla p^{\frac{1}{2}} = \frac{1}{2}\left(\nabla p^0 + \nabla p^1 \right) \tag{33}$$

After computing $\nabla p^{\frac{1}{2}}$, the sequence is to solve (21) to obtain U^* followed by solving equation (22) to obtain U^2. Equation (28) is then solved to find $\nabla \tilde{p}^{\frac{1}{2}}$ and used in (27) to find $\nabla p^{\frac{3}{2}}$. The process repeats to find U^3 by first solving (28) to find $\nabla \tilde{p}^{\frac{5}{2}}$, using this to obtain $\nabla p^{\frac{5}{2}}$, and solving equations (21) and (22) to find U^3. The process continues until the desired end-state is achieved.

C. SOLVING POISSON'S EQUATION IN A SEMI-PERIODIC REGION

Poisson's equation needs to be solved every time one uses the projection method. The specific problem we are interested in involves a Poisson's equation in a semi-periodic domain. That is, the solution is only periodic in the x-direction; not in the y-direction.

Consider the following problem:

$$\begin{cases} \Delta\phi(x,z) = f(x,z), (x,z) \in D = [0,\ L]\times[0,\ H], \\ f(x,z), \phi(x,z) \text{ are periodic in x-direction with period } L \\ \phi(x,z) \text{ satisfies Neumann boundary conditions at z} = 0,\ H \end{cases} \tag{34}$$

Where Neumann boundary conditions are those that give vanishing normal derivatives on the boundaries, and where the length and height of the domain are $L=1$, and $H=5$. Now suppose grid points in region D are at $\{(x_i, y_j),\ i=1,2,...,Nx;\ j=1,2,...,Ny\}$. It is important to note here that $x_{Nx} = L - \Delta x$. In application of Fourier spectral methods, the sums that one must evaluate are given by equations (35) and (36).[21]

[21] Canuto, Hussaini, Quarteroni, and Zang, ***Spectral Methods in Fluid Dynamics***, (New York: Springer-Verlag, 1988): 500.

$$\hat{\phi}(k, j) = \frac{1}{Nx}\sum_{l=1}^{Nx}\phi(l, j)e^{-2\pi i(l-1)k/Nx}, k = -\tfrac{Nx}{2}, ..., \tfrac{Nx}{2}-1;\ j \text{ fixed} \tag{35}$$

and

$$\phi(l, j) = \sum_{k=-\frac{Nx}{2}}^{k=\frac{Nx}{2}-1}\hat{\phi}(k, j)e^{2\pi i(l-1)k/Nx},\ l = 1,\ ..., Nx \tag{36}$$

It is apparent that for any integers p and k, $\hat{\phi}(k + pNx, j) = \hat{\phi}(k, j)$ holds. .

When the array $\left(\hat{\phi}(1, j), \hat{\phi}(2, j), ..., \hat{\phi}(Nx/2-1, j), \hat{\phi}(-Nx/2+1, j),\ ..., \hat{\phi}(-1, j)\right)$ is fed into the Fourier transform to find $\hat{\phi}$, it returns the array $Nx\cdot\left(\hat{\phi}(0, j), \hat{\phi}(1, j), ..., \hat{\phi}(Nx/2-1, j), \hat{\phi}(-Nx/2, j), \hat{\phi}(-Nx/2+1, j), ..., \hat{\phi}(-1, j)\right).$ Conversely, when this array is fed into the standard FFT (without the Nx factor) for evaluating ϕ, the array $\left(\phi(1, j), \phi(2, j), ..., \phi(Nx, j)\right)$ is returned.

Now back to the cell-centered grids where the mesh points are $(x_i, z_j),\ i = 2, \cdots,\ Nx+1,\ j = 2,\ Nz+1$. First use the standard five-point stencil to make the Poisson's equation discrete:

$$D^+D^-\phi = f\ , \tag{37}$$

Then taking the discrete Fourier transform with respect to x of equation (37) yields:

$$\frac{\hat{\phi}(k, j+1) - 2\hat{\phi}(k, j) + \hat{\phi}(k, j-1)}{(\Delta z)^2} + \frac{2(\cos 2\pi k/Nx - 1)}{(\Delta x)^2}\hat{\phi}(k, j) = \hat{f}(k, j),\ j = 2, ..., Nz+1 \tag{38}$$

with Neumann boundary conditions

$$\hat{\phi}(k, 1) = \hat{\phi}(k, 2),\ \hat{\phi}(k, Nz+2) = \hat{\phi}(k, Nz+1) \tag{39}$$

Now equation (38) with (39) forms a tridiagonal system for each fixed k:

$$\begin{bmatrix} c-1 & 1 & & & \\ 1 & c-2 & 1 & & \\ & \ddots & \ddots & \ddots & \\ & & 1 & c-2 & 1 \\ & & & 1 & c-1 \end{bmatrix} \begin{bmatrix} \hat{\phi}(k,2) \\ \hat{\phi}(k,3) \\ \vdots \\ \hat{\phi}(k,Nz) \\ \hat{\phi}(k,Nz+1) \end{bmatrix} = (\Delta z)^2 \cdot \begin{bmatrix} \hat{f}(k,2) \\ \hat{f}(k,3) \\ \vdots \\ \hat{f}(k,Nz) \\ \hat{f}(k,Nz+1) \end{bmatrix} \tag{40}$$

where

$$c = \frac{2\cos(2\pi k / Nx - 1)(\Delta z)^2}{(\Delta x)^2} \tag{41}$$

and $k = \frac{-Nx}{2}, \ldots, \frac{Nx}{2} - 1$.

When $c \neq 0$, the matrix A in (40) is nonsingular (i.e. the determinant $\neq 0$) (note c<0 and –A is strictly diagonally dominant) and one can use the Crout factorization method.

When $c = 0$, the matrix A in (40) is singular; which is consistent with the fact that the Poisson equation with homogeneous Neumann boundary conditions is unique; only to an additive arbitrary constant. In general, to solve

$$\begin{bmatrix} -1 & 1 & & & \\ 1 & -2 & 1 & & \\ & \ddots & \ddots & \ddots & \\ & & 1 & -2 & 1 \\ & & & 1 & -1 \end{bmatrix} \begin{bmatrix} x_1 \\ x_2 \\ \vdots \\ x_{n-1} \\ x_n \end{bmatrix} = \begin{bmatrix} b_1 \\ b_2 \\ \vdots \\ b_{n-1} \\ b_n \end{bmatrix}, \tag{42}$$

one has,

$$\begin{bmatrix} -1 & 1 & & & \\ 0 & -1 & 1 & & \\ & \ddots & \ddots & \ddots & \\ & & 0 & -1 & 1 \\ & & & 0 & 0 \end{bmatrix} \begin{bmatrix} x_1 \\ x_2 \\ \vdots \\ x_{n-1} \\ x_n \end{bmatrix} = \begin{bmatrix} b_1 \\ b_1 + b_2 \\ \vdots \\ b_1 + \cdots + b_{n-1} \\ b_1 + \cdots + b_n \end{bmatrix} \tag{43}$$

where

$$b_1 + \cdots + b_n = 0 \tag{44}$$

and x_n is arbitrary. Without loss of generality, if we assume

$$x_n = 0, \tag{45}$$

then

$$\begin{aligned} x_{n-1} &= x_n - (b_1 + \cdots + b_{n-1}) \\ x_{n-2} &= x_{n-1} - (b_1 + \cdots + b_{n-2}) \\ &\cdots \\ x_1 &= x_2 - b_1 \end{aligned}$$

Once the solution to (40) is found, apply the inverse Fourier transform to

$$\hat{\phi}(k, j),\ j \text{ fixed} \tag{46}$$

to recover $\phi(i, j)$. Having solved for ϕ, U^* can be determined leading to the calculation of U^{n+1} covered in Section B.

D. NUMERICAL METHODS FOR THE WEAKLY COMPRESSIBLE MODEL

The projection method is used to solve (18) and (19), the weakly compressible model, with cell-centered grids.

Now we give an outline of the numerical methods used to solve the weakly compressible equations (18) and (19) in a semi-periodic region.

First we need to project a suggested velocity field to obtain a divergence-free initial velocity field. For example, let us take the standard cellular flow initial condition for the velocity field $U = (\vec{u}, \vec{v})$ as

$$u_0(x,z) = \cos(2\pi x)\sin(2\pi z), \tag{47}$$

$$v_0(x,z) = -\sin(2\pi x)[\cos(2\pi z) - 1], \tag{48}$$

where $x \in [0,1], z \in [0, Z_L]$ (the choice of Z_L depends on how many vortices one wants in the vertical direction. When L is not 1, you have to be careful with the time step. In this study $L = 5$. This velocity field is projected to obtain a divergence-free initial velocity U^0. More specifically

$$\Delta\phi = DU \tag{49}$$

is solved and then

$$U^0 = U - \nabla\phi \tag{50}$$

where D and ∇ are discrete divergence and gradient operators. This is equivalent to the step used in solving the incompressible Navier-Stokes equation, (20). The solution to equation (49) is outlined in Section C, entitled Solving Poisson's Equation in a Semi-Periodic Region.

The second step solves for ∇p^0:

$$(I - \mathrm{P})\overline{U} = \nabla p^0, \tag{51}$$

where

$$\overline{U} = -[h(z)(U\cdot\nabla)U]^0 - \left[h'(z)\begin{pmatrix} uv \\ v^2 \end{pmatrix}\right]^0 + \frac{1}{Re\cdot h(z)}\Delta(h(z)U^0) - \frac{\mathrm{g}}{h(z)}\hat{k}. \tag{52}$$

In other words, solve

$$\Delta\phi = D\bar{U} \tag{53}$$

and then set

$$\nabla p^0 = G\phi\,. \tag{54}$$

The third step of the numerical process uses Euler's method to find U^1:

$$U^1 = U^0 + \Delta t(-\nabla p^0 + \bar{U}). \tag{55}$$

The forth step determines ∇p^1 in the same way as ∇p^0 was found. The only difference is in replacing U^0 with U^1.

$$(I - \mathrm{P})\bar{U} = \nabla p^1, \tag{56}$$

where

$$\bar{U} = -[h(z)(U\cdot\nabla)U]^1 - \left[h'(z)\begin{pmatrix} uv \\ v^2 \end{pmatrix}\right]^1 + \frac{1}{Re\cdot h(z)}\Delta(h(z)U^1) - \frac{\mathrm{g}}{h(z)}\hat{k}. \tag{57}$$

The fifth part of the sequence is to average ∇p^0 and ∇p^1 to find $\nabla p^{\frac{1}{2}}$:

$$\nabla p^{\frac{1}{2}} = \frac{1}{2}(\nabla p^0 + \nabla p^1) \tag{58}$$

as was done in bootstrapping the Navier-Stokes projection method of part B.

The final step of the sequence is to loop through the steps until a stopping criterion is satisfied. The loop consist of determining

$$[(U\cdot\nabla)U]^{n+\frac{1}{2}} \approx \frac{1}{2}(3H^n - H^{n-1}) \tag{59}$$

where

$$H^n = [(U\cdot\nabla)U]^n, \tag{60}$$

employing the Navier-Stokes equation to compute U^* from

$$\frac{U^* - U^n}{\Delta t} = -\nabla p^{n-\frac{1}{2}} - h(z)[(U \cdot \nabla)U]^{n+\frac{1}{2}} + \frac{\nu}{h(z)} \frac{\Delta h(z)(U^n + U^*)}{2} + \frac{\mathrm{g}}{h(z)}; \tag{61}$$

projecting U^* to obtain U^{n+1}:

$$U^{n+1} = \mathrm{P}(U^*), \tag{62}$$

by solving

$$\Delta \phi = DU^*, \tag{63}$$

and setting

$$U^{n+1} = U^* - \nabla \phi; \tag{64}$$

and finally updating the pressure gradient according to

$$\nabla p^{n+\frac{1}{2}} = \nabla p^{n-\frac{1}{2}} + \frac{1}{\Delta t}(I - \mathrm{P})U^*. \tag{65}$$

This concludes the calculation for the weakly compressible model. We will see in the results chapter that the addition of a altitude dependent density profile, creating a weakly compressible model, does affects the numerical results.

E. TIME STEP CONTROL AND BOUNDARY CONDITIONS

Choosing an appropriate time step is crucial to the stability of the numerical algorithm. The time step has already been increased significantly due to neglecting high frequency oscillation of the fluid as are present when acoustic phenomenon are modeled. Because we are using a standard centered-difference scheme for the viscous term of the Navier-Stokes equation, our time step is restricted by

$$\frac{\Delta t}{Re\Delta x^2} < 1. \tag{66}$$

On the other hand, the Courant-Friedrichs-Lewy (CFL) condition requires

$$\max\left|\frac{U\cdot\Delta t}{\Delta x}\right| \le C \tag{67}$$

where the choice of C depends on the ODE solver, employed in the time marching scheme. For our case, the weakly compressible problem, as α increases, the coefficient of the convective term also increases and the time step factor mush be reduced by a factor of about $e^{\alpha-1}$.

In general, if we want $\Delta t \sim \Delta x$, (66) requires that

$$N = \frac{1}{\Delta x} < Re \tag{68}$$

which will result in an under resolved problem if Re is too small. If for example $Re = 100$, and $N = 128$, the iterations in solving for U^* do not converge and the method fails.

Boundary conditions are always an issue when solving differential equations of any kind. Our study employs periodic boundary conditions in the x-direction and a simple reflection, or linear interpolation to satisfy the no-flow boundary condition. However, some of the following problems may arise:

- Lower order accuracy in calculating the velocity gradient at the boundary

Consider a special case where the flow is Poiseuille flow:

$$u = z(z-1), \tag{69}$$

$$v = 0. \tag{70}$$

Using cell-centered grids with grid size h, we have

$$\vec{u}_1 = h/2\left(h/2 - 1\right), \tag{71}$$

$$\vec{u}_{-1} = -\vec{u}_1 . \tag{72}$$

So the numerical approximation to the derivative $\frac{\partial \vec{u}}{\partial z}$ at the boundary is

$$\frac{\vec{u}_1 - \vec{u}_{-1}}{2h/2} = h/2 - 1, \tag{73}$$

while the exact solution of $\frac{\partial \vec{u}}{\partial z}$ is -1. This shows that the order at the boundaries is first-order; one order lower than the interior which has second-order.

- Pressure gradient boundary layer

Note that at the boundary the following is true

$$U^{n+1} = U^* - \nabla\phi, \tag{74}$$

$$U^{n+1} = 0, \tag{75}$$

$$U^* = 0. \tag{76}$$

From these truths we conclude

$$\nabla\phi = 0, \tag{77}$$

at the boundary which in turn leads to

$$\nabla p^{n+\frac{1}{2}} = \nabla p^{n-\frac{1}{2}} \tag{78}$$

at the boundary, so ∇p will be unchanged at the non periodic boundaries.

Long time behavior of the analysis creates problems also. This study ran the code for a final scaled time of

$t = 7.0$. One of the runs developed holes (areas of the medium where calculations could not be obtained in the numerical analysis) in the data when it ran for this long. In general the magnitude of the velocity is what needs to be looked at to see if there will be a problem with long term behavior. The code needs to be stopped when the flow size, or magnitude of the velocity is less than the grid size (i.e. $\max(\Delta x, \Delta y)$).

Other numerical methods could provide a remedy for this malignant longtime behavior. Our method only utilized a second order calculation. One could use a multi-grid method to solve Poisson's equation coupled with a Runge-Kutta method for the time marching, which could achieve a higher order truncation error and therefore provide better results.

THIS PAGE INTENTIONALLY LEFT BLANK

III. NUMERICAL RESULTS

This study documents phenomena directly attributable to the anelastic fluid equations. In this section numerical results are displayed and discussed for the zero-gravity anelastic system (12) and (13) , and a zero-gravity Navier-Stokes equation modeling incompressible flow. Specifically, the fluid flow geometries and effect of weak compressibility are explored.

The evolutions of ten different systems are going to be studied. Within those ten, there are three separate initial conditions studied.

$$\begin{aligned} u_0(x,z) &= \cos(2\pi x) * \sin(2\pi z) \\ v_0(x,z) &= -\sin(2\pi x) * (\cos(2\pi z) - 1) \end{aligned} \tag{79}$$

$$\begin{aligned} hh &= x + \varepsilon * \sin(\pi x) * (1 - \tanh^2(\delta(z - Z_L/2))) \\ u_0(x,z) &= \cos(2\pi hh) * \sin(2\pi z) \\ v_0(x,z) &= -\sin(2\pi hh) * (\cos(2\pi z) - 1) \end{aligned} \tag{80}$$

$$\begin{aligned} u_0(x,z) &= z * (Z_L - z) \\ v_0(x,z) &= 0 \end{aligned} \tag{81}$$

These systems of equations describe the initial conditions evaluated in the study. Equation (79) represents the standard cellular flow equation. Equation (80) is similar to the standard cellular flow equation, except it has a perturbed middle region. This region is supplied by the hh term, which distorts the middle vortex of the medium as seen in Figure 5. The last initial condition, (81) is Poiseuille flow and an exact solution to Euler's equation. Because Poiseuille flow does not have a vertical component of velocity, results are not as "rich" as found in the first two cases.

Figures 5, 6, and 7 give a visual display of the three initial conditions explored in this study. The vector field is shown on the right and the vorticity field on the left in each instance. The governing equations have been non-dimensionalized. Therefore, the numbers given on the colorbar (shown in the middle of the figure) to quantify the vorticity are likewise non-dimensional. The darker colors indicate stronger vortices which in turn imply stronger velocity fields.

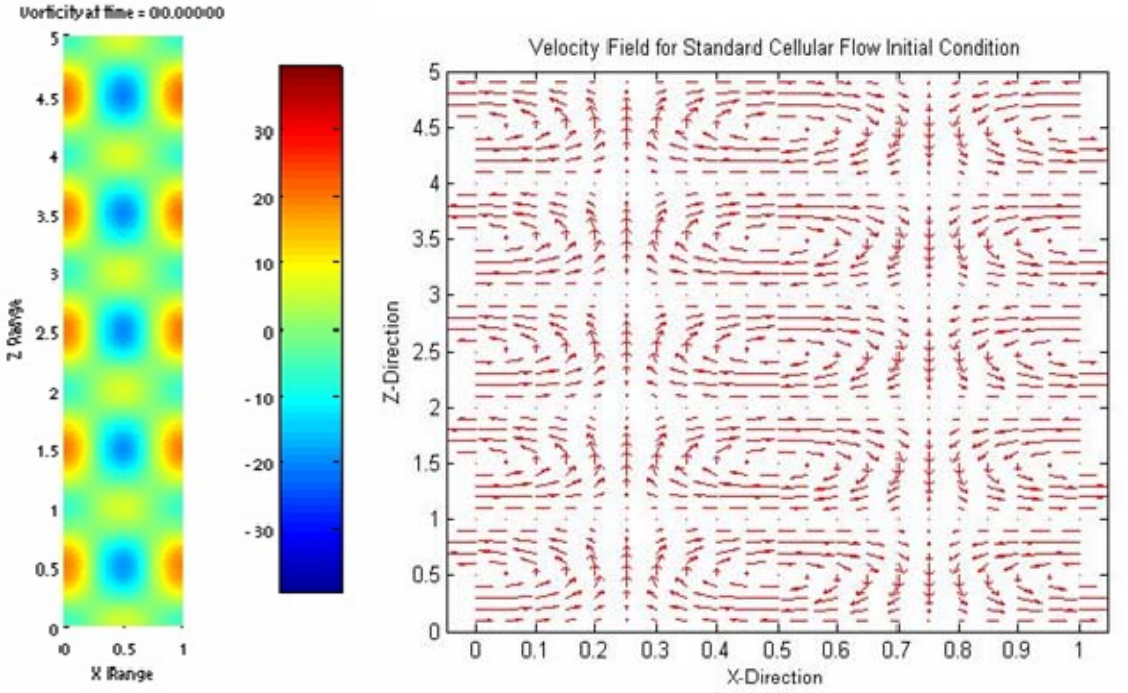

Figure 5. Standard cellular flow initial condition shown in colored vortex scheme and vector field.

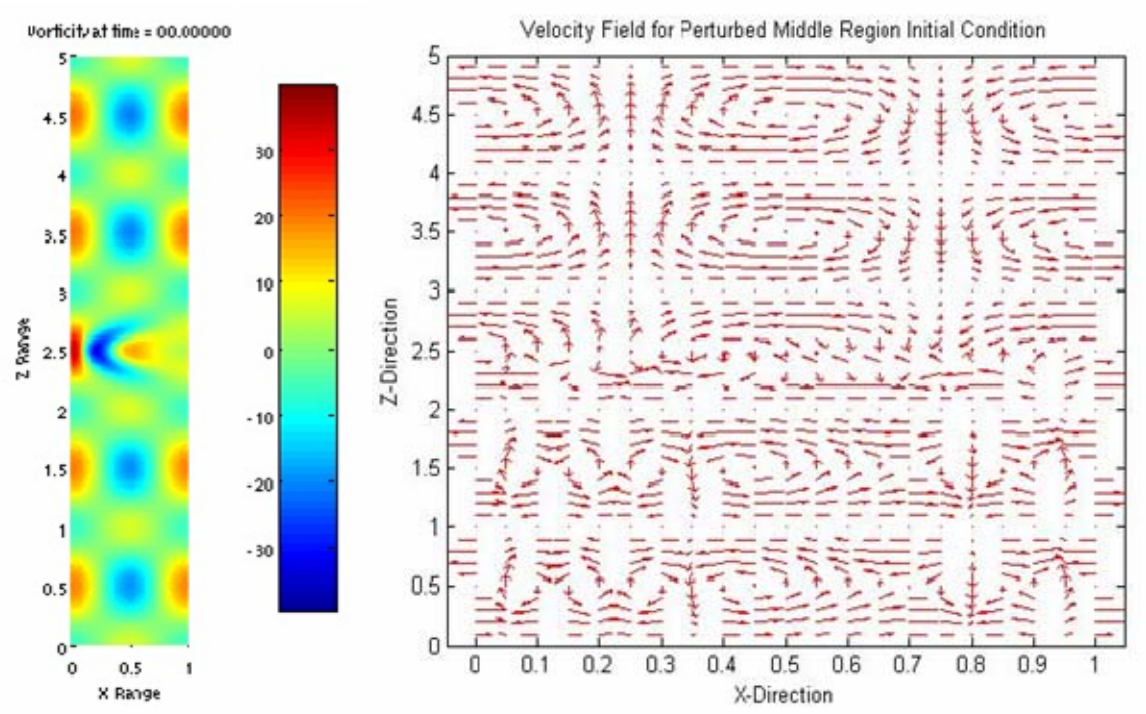

Figure 6. Perturbed middle region initial condition in colored vortex scheme and vector field.

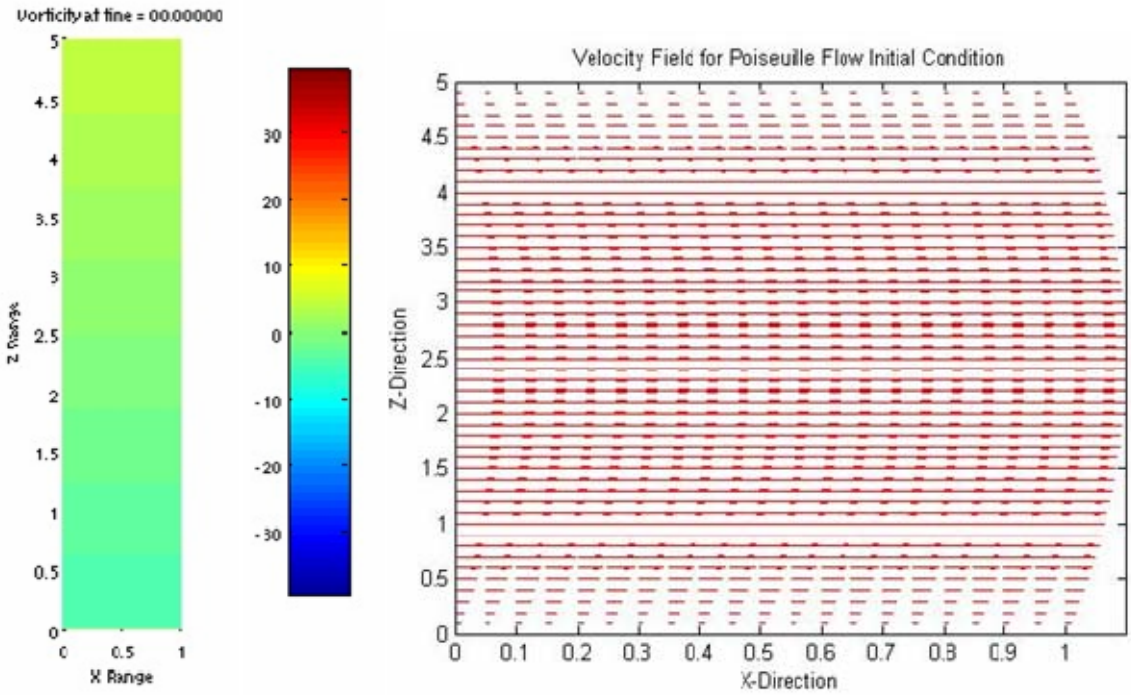

Figure 7. Poiseuille flow initial condition in colored vortex scheme and vector field.

The initial conditions do not affect the compressibility, be it weakly compressible or incompressible, but do supply the numerical analysis with a starting point. However, it is shown that variations of the initial conditions do affect the output produced by the numerical methods employed.

The results shown do not display interim or steady-state velocity fields. Instead, the vorticity of the fluid within the medium is displayed. The vorticity is defined as the cross product of the directional velocity and the gradient operator corresponding to the fluid rotation, is given in equation (82).

$$\nabla \times \vec{u} = \begin{vmatrix} \vec{i} & \vec{j} & \vec{k} \\ \frac{\partial}{\partial x} & \frac{\partial}{\partial z} & 0 \\ \vec{u} & \vec{v} & 0 \end{vmatrix} \tag{82}$$

where x is the horizontal direction, z is the vertical direction, u is the horizontal velocity, and v is the vertical velocity. Two of the blocks are equal to zero because the problem is two dimensional. In this way, the vorticity of the flow is represented by a vector with a single nonzero component in the direction perpendicular to the x-z plane.

A. INCOMPRESSIBLE MODEL

1. Stream Function Initial Condition

The first results observed are those generated by the incompressible model, utilizing equations (12) and (14). The vorticity magnitudes at three time steps using the standard cellular flow initial condition are shown in Figure 8.

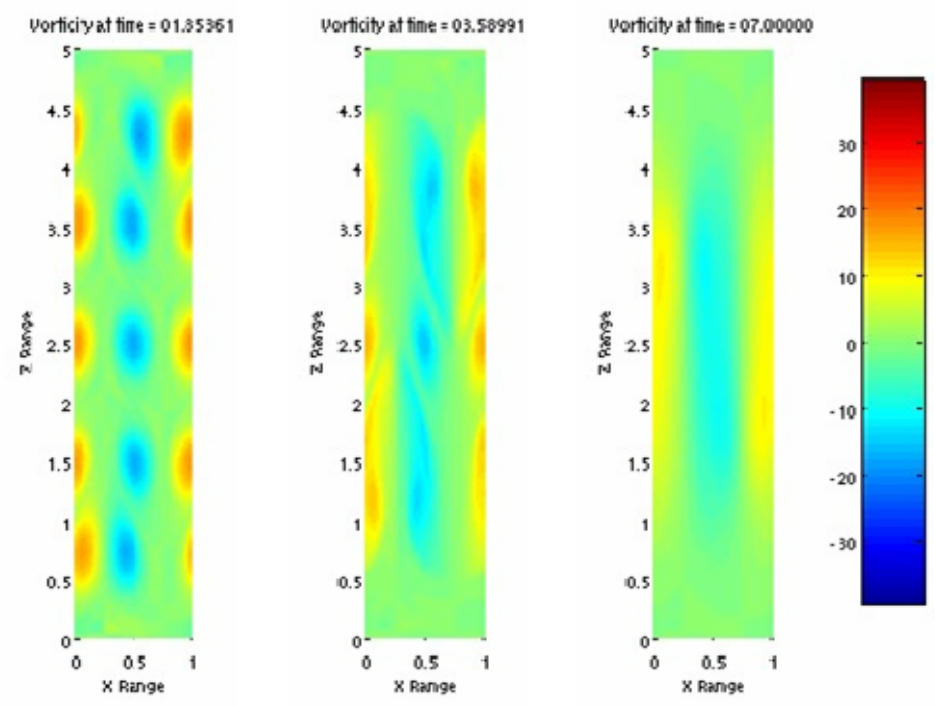

Figure 8. Incompressible model with a standard cellular flow initial condition.

Figure 8 demonstrates that the cellular flow initial condition governed by the Navier-Stokes equation, forces the five individual vortices to combine pair wise into new single vortices. When these combined vortices reach the center of the medium, the two outermost ones interact with the two closer to the middle of the region producing a new vortex pair. Ultimately, the middle vortex is absorbed and an eddy is created.

It can also be observed that the anelastic model is allowing mixing through exchanges of fluids from the lower half of the computational domain to the upper half, and vice versa. Analyzing large scale fluid mixing is often studied by researchers. using just such anelastic simulations as done here.

2. Perturbed Middle Region Initial Condition

The perturbed middle region initial case results in a more chaotic flow development. It is observed that this initial condition disables the individual vortices from combining as they do in the cellular flow initial condition case just described.

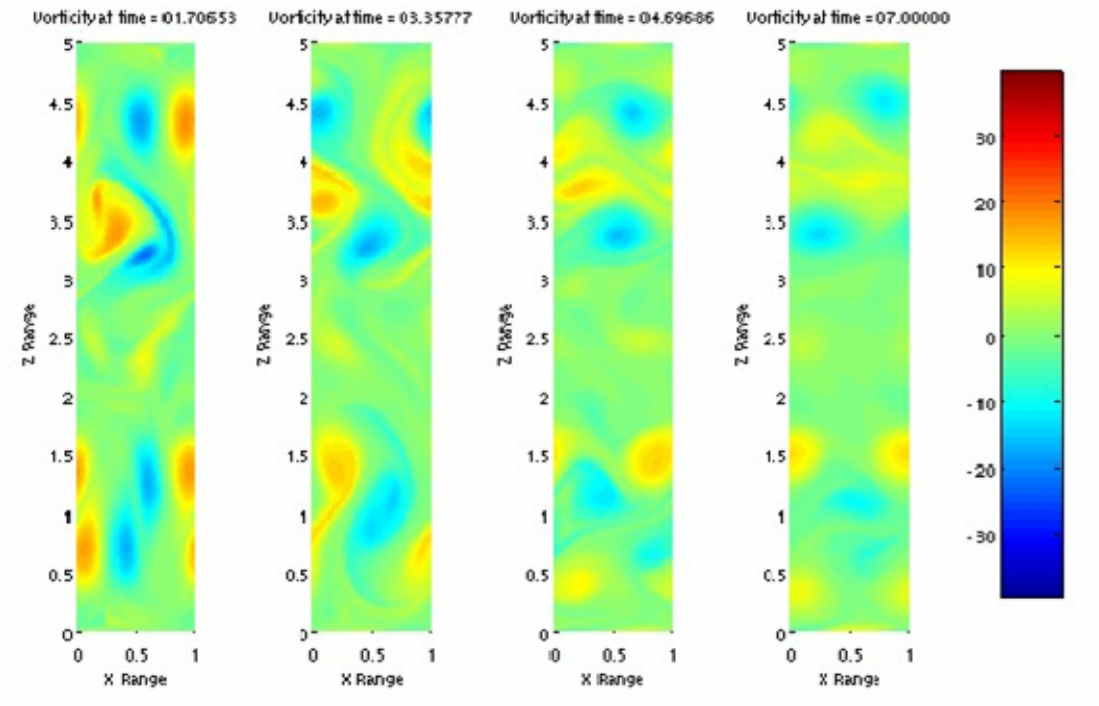

Figure 9. Results of perturbed middle region initial condition with Navier-Stokes equation.

The results indicate there is not the same amount of vortex pairing as occurred in the first set of results. Figure 9 shows that there is some initial pairing of vortices. However, after $t \approx 2$, no further mixing occurs, and the vortices tend to separate. It appears that fluids from the top of the modeled region to the bottom are separated by something akin to a mixing barrier formed at

the center of the z-axis. Also noted, is a lack of horizontal mixing, which coincides with the cellular initial condition results.

3. Poiseuille Flow Initial Condition

The Poiseuille flow initial condition case is essentially unidirectional flow with no vertical velocity component. Because of this the non linear terms in the Navier-Stokes equation vanish, resulting in a flow that maintains its profile while slowing down due to viscous effects. Bear in mind that gravitational effects have been neglected in the analysis.

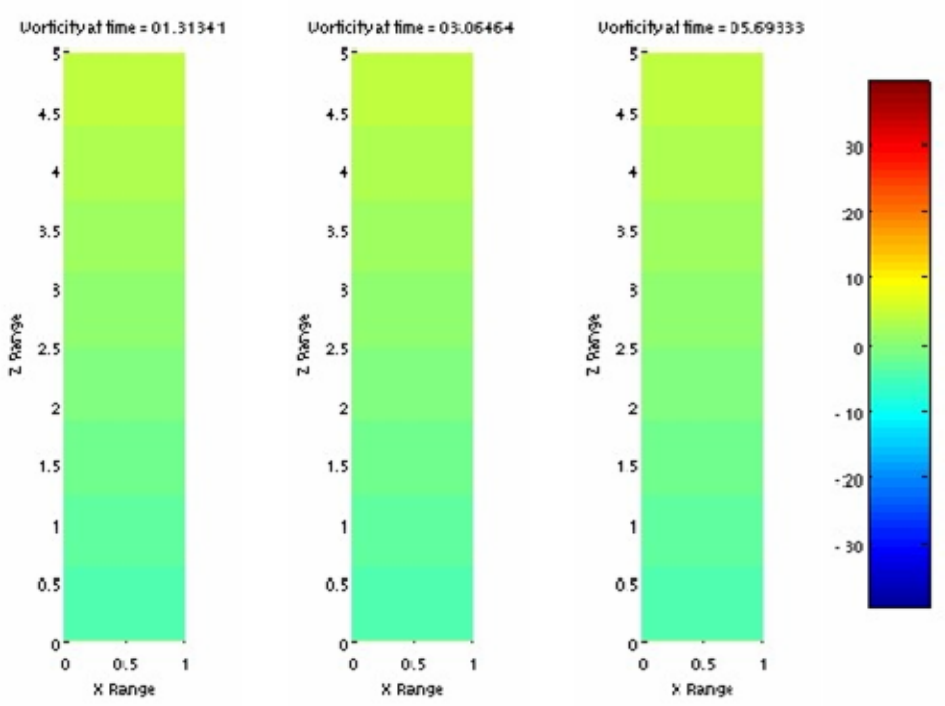

Figure 10. Poiseuille flow initial condition computed with incompressible Navier-Stokes equations and a colorbar showing magnitude of velocity.

No changes exist in the flow of the fluid over time other than a slight slowing down of the fluid speed as would be expected analytically. It can be seen in Figure

10 that the fluid appears to be stationary with no exchange of fluids vertically throughout the medium.

B. WEAKLY COMPRESSIBLE MODEL

1. Stream Function Initial Condition

a. Exponential Density Profile

This simulation involves a non-structured, exponential density profile, $\rho(z) = e^{-\alpha z}$, where α is any constant and z is the vertical distance of the atmosphere. This model simulates the most typical mean state profile in the atmosphere that accounts for gravity to compress an ideal gas under its own weight. This study analyzes the affect of an increasing α on the numerical calculations. $\alpha = .02,\ \alpha = .05,$ and $\alpha = .1$ are all investigated within this study.

1. $\alpha = .02$ in the exponential density profile.

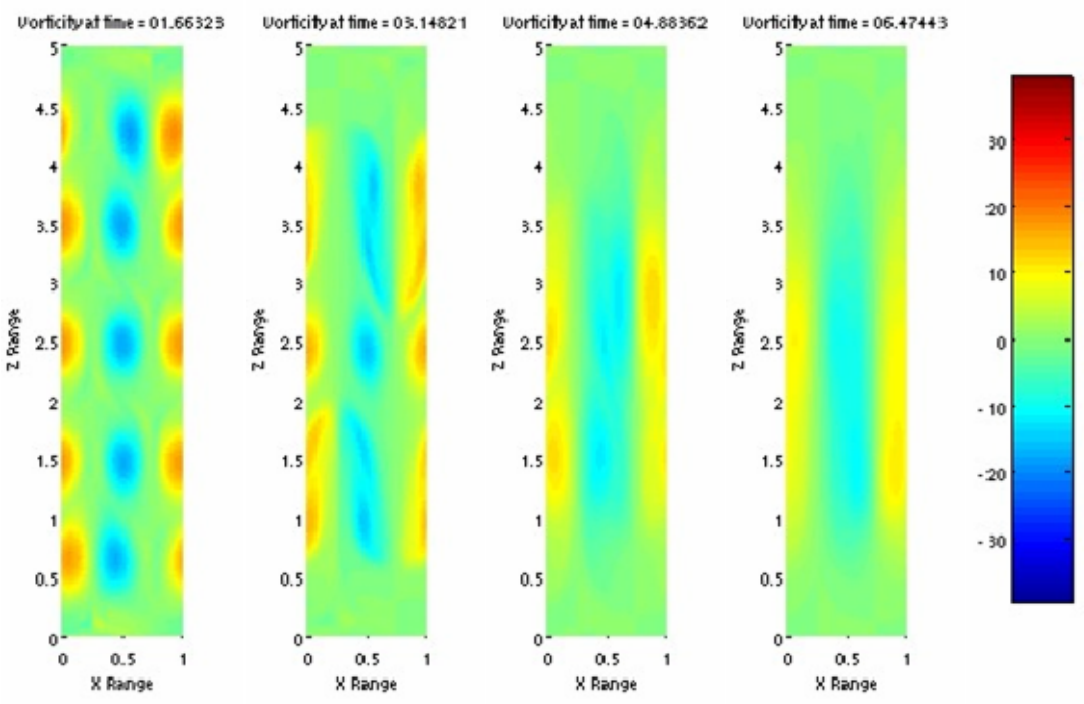

Figure 11. Results for cellular flow initial condition with an exponential density profile and $\alpha = .02$.

As seen in Figure 11, the flow qualitatively looks similar to that of the incompressible Navier-Stokes simulation, Figure 8. Vortices in the respective upper and lower regions merge together, finally merging with the middle vortex to form an eddy that allows for vertical mixing. However, it is noted that the exponential density profile does cause a vertical shift downward in the flow. The final eddy in the incompressible case is bounded vertically by z=4 and z=1, while the eddy in the weakly compressible case is bounded vertically by z=3.5 and z=1.0.

2. $\alpha = .05$ in the exponential density profile.

Figure 12, shown below, displays the affects of increasing α in the weakly compressible model. It is observed that, similar to when $\alpha = .02$, there is a pairing of outer vortices; which merge into a single eddy as time proceeds. One difference is the downward motion of the mixing layer with increasing α. Note that the two vortices on the top merge before those at the bottom. An eddy is being formed, but there is a small mixing barrier at z=1.5 that does not allow vertical mixing.

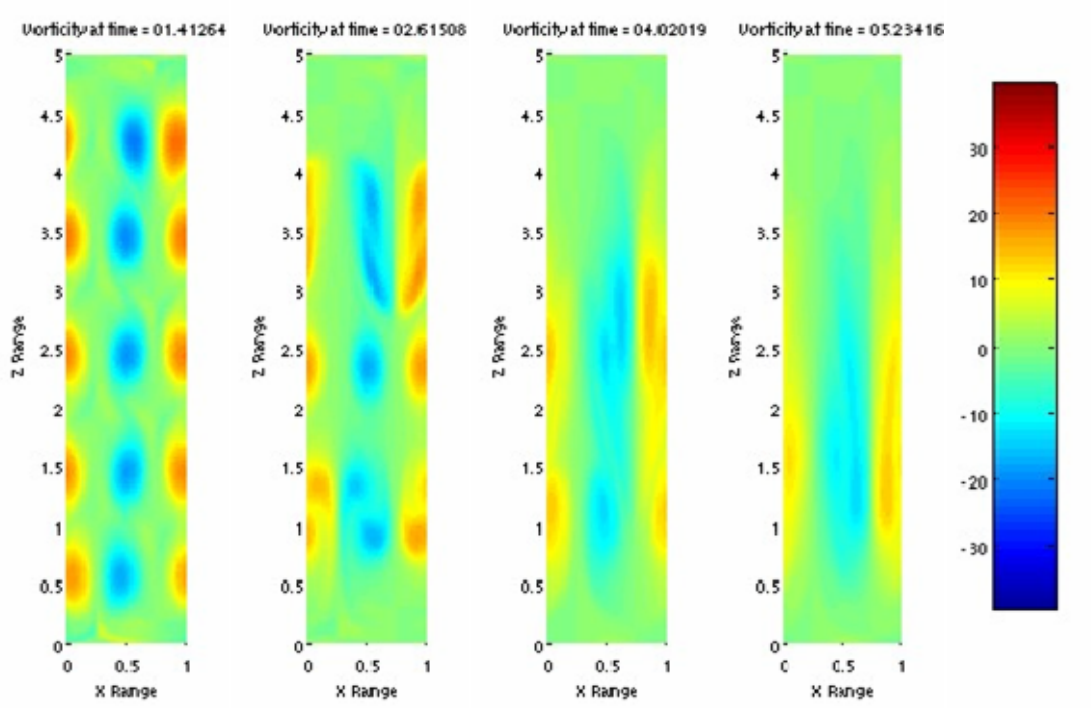

Figure 12. Results for cellular flow initial condition with an exponential density profile and $\alpha = .05$.

3. $\alpha = .1$ in the exponential density profile.

These results for $\alpha = 0.1$ are shown in Figure 13, but may not be reliable for conclusions. Again, as in the results for $\alpha = .05$, there is a vertical movement of the fluid. However, in this model the grouping of pairs occurs very quickly and rapidly plummets to the bottom of the medium. The flow does not weaken as quickly as it does for the other runs and once it reaches the bottom there is no further large scale movement of fluid.

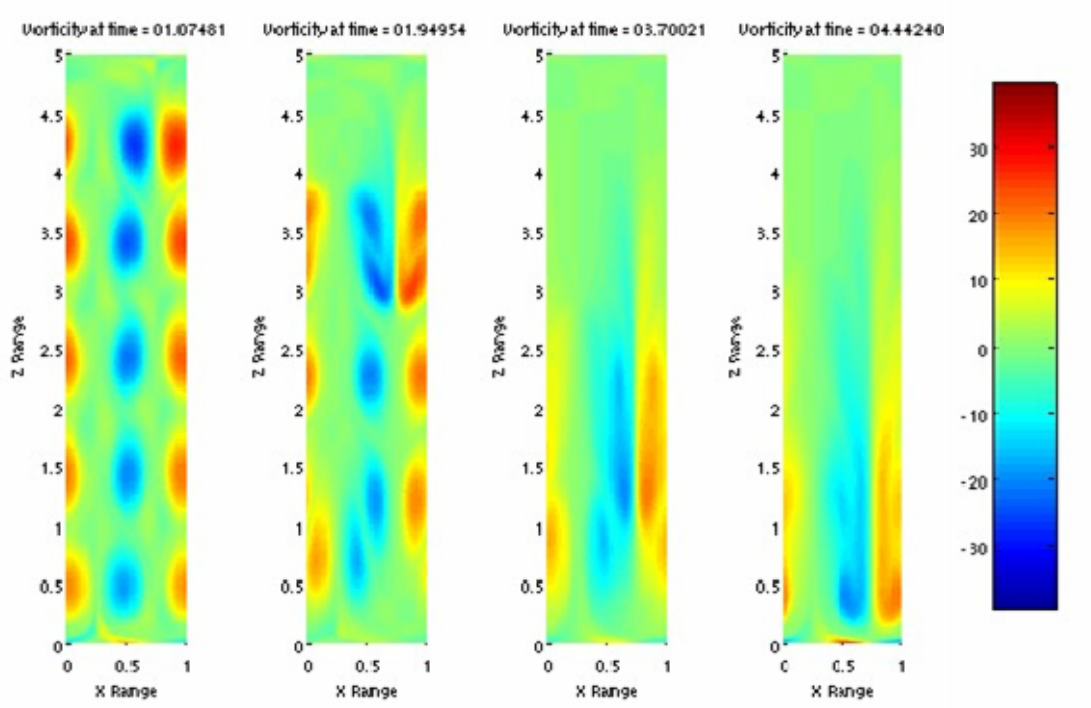
Vorticity at time = 01.07481
Vorticity at time = 01.94954
Vorticity at time = 03.70021
Vorticity at time = 04.44240
Z Range
X Range

Figure 13. Results for standard cellular flow initial condition with an exponential density profile and $\alpha = .1$.

b. Hyperbolic Tangent Density Profile

This part of the study incorporates a structured background density profile with an imbedded transition layer of the form of $1/\rho(z) = 1 + \varepsilon \cdot \tanh[\delta(z - Z_L/2)]$. Here, a mixing barrier is formed limiting vertical fluid exchange. The phenomenon of outside pairs grouping first and then coming to the center no longer occurs. Figure 14 shows during the downward flow, the top two vortices do pair, but the bottom two pair simultaneously with the middle vortex, which moves down to meet the other two. This forms a mixing barrier at z=2.5, unlike that of the incompressible Navier-Stokes results.

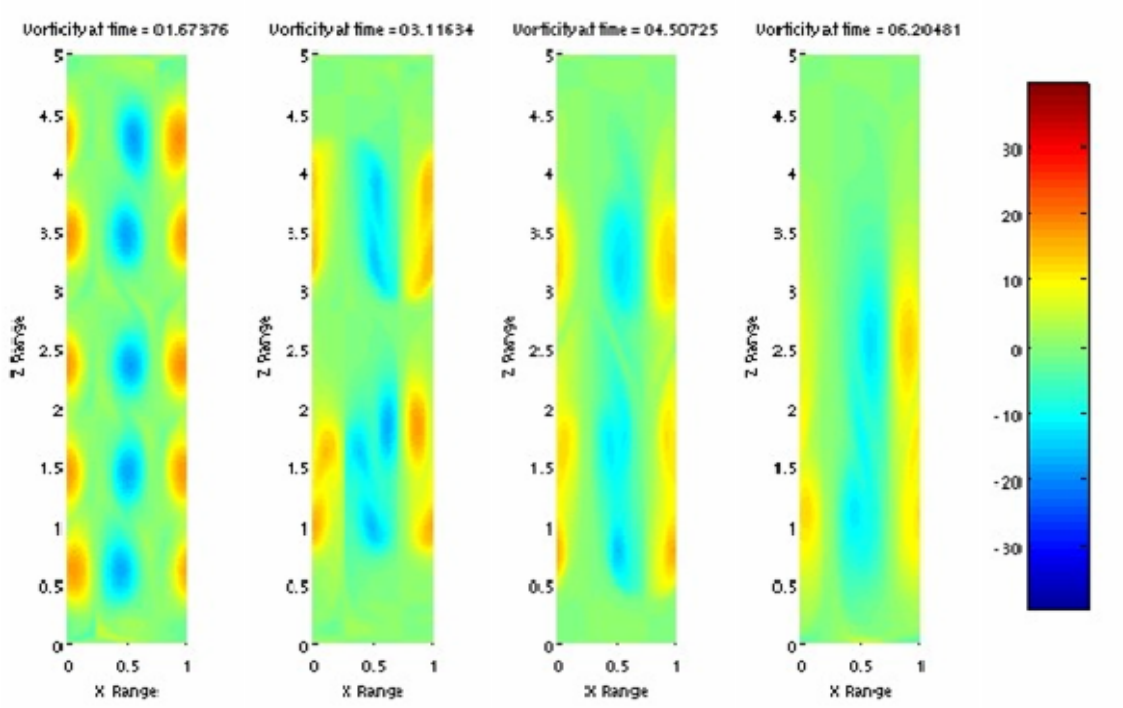

Figure 14. Weakly compressible system with standard cellular flow and hyperbolic tangent density profile.

c. Linear Density Profile

This part of the study was done using the standard cellular flow initial condition and a linear density profile, $\rho(z) = a \times z + 1.0$, where a is a constant. The results of the cellular flow initial condition and the linear density profile with $a = -0.02$ are shown in Figure 15, below. It is known that for small α the exponential function looks very much like a straight line. Because we are using a small alpha and our range and domain are small, the exponential in this study does look act like a straight line. As is seen in Figure 15, the numerical results for the linear density profile are similar to the results for a weakly compressible model with an exponential density profile given a small alpha. An eddy is formed, but compared to the incompressible model the eddy is shifted downward.

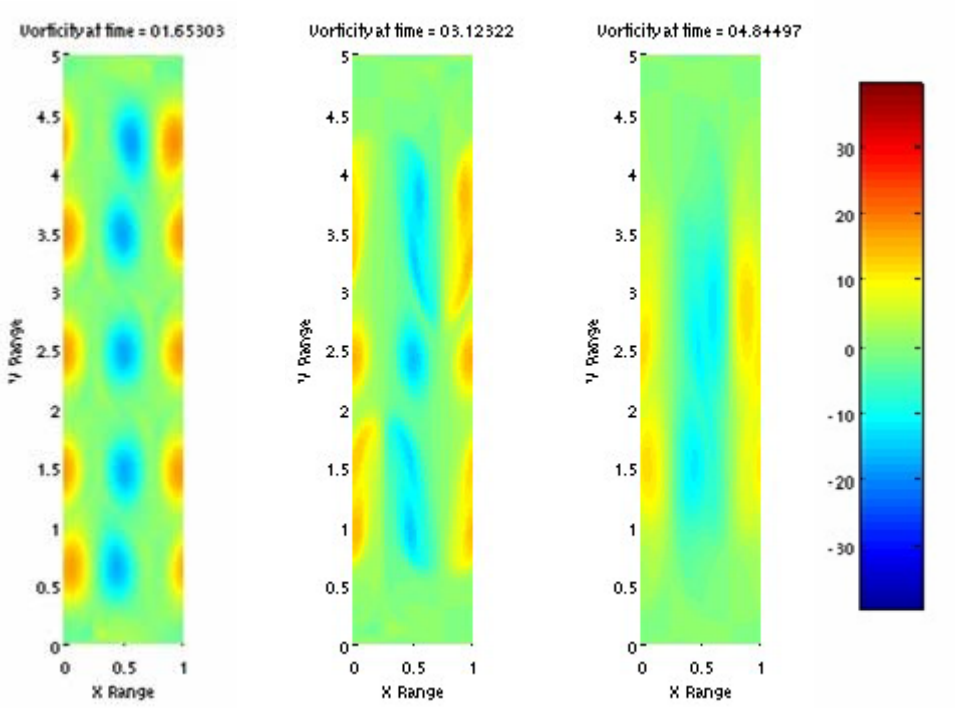

Figure 15. Results of standard cellular flow initial condition with a linear density profile.

2. Perturbed Middle Region Initial Condition

a. Exponential Density Profile

1. $\alpha = .02$ in the exponential density profile

This study exhibits the affects of a perturbed middle region initial conditions on the anelastic equations. The output, seen in figure 16, shows a significant difference in fluid flow from the output using the standard cellular flow initial condition. However, there is an uncanny similarity between the incompressible Navier-Stokes run with the perturbed middle region and this set of results. The perturbed middle region does not allow vortices to merge and to eventually and form an eddy. Instead, it appears the bottom two vortices begin to merge, but then weaken and diverge to become individual cells once again. In all of this, it seems that a mixing barrier has

been created in the center, comparable to that of the incompressible Navier-Stokes analysis.

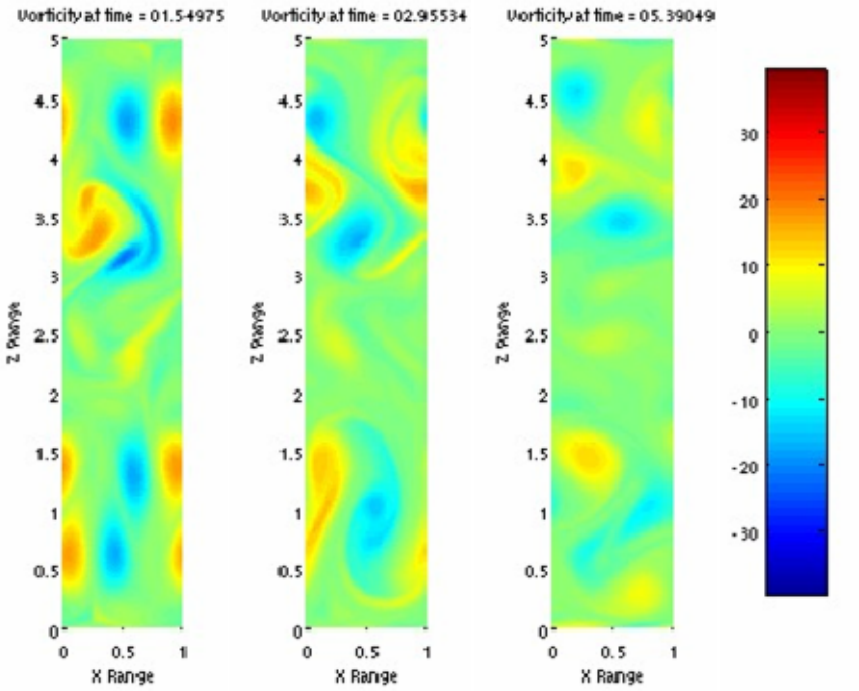

Figure 16. Numerical Results for perturbed middle region initial condition with $\alpha = .02$ in the exponential density profile.

2. $\alpha = .05$ for exponential density profile.

The affect of increasing the α term in the exponential density profile using again the perturbed middle region initial conditions are displayed in Figure 17. Here, increasing α from 0.02 to 0.05 has a slight affect on the vortex flow. It appears that the increases in α allow for a slower process to occur. At the final time in this run the fluids are stronger (darker color) than they are at the end of the $\alpha = .02$ run. Pairing still occurs and a separation of vortices with a mixing barrier forms, that again restricts vertical fluid exchange in the center of the fluid domain.

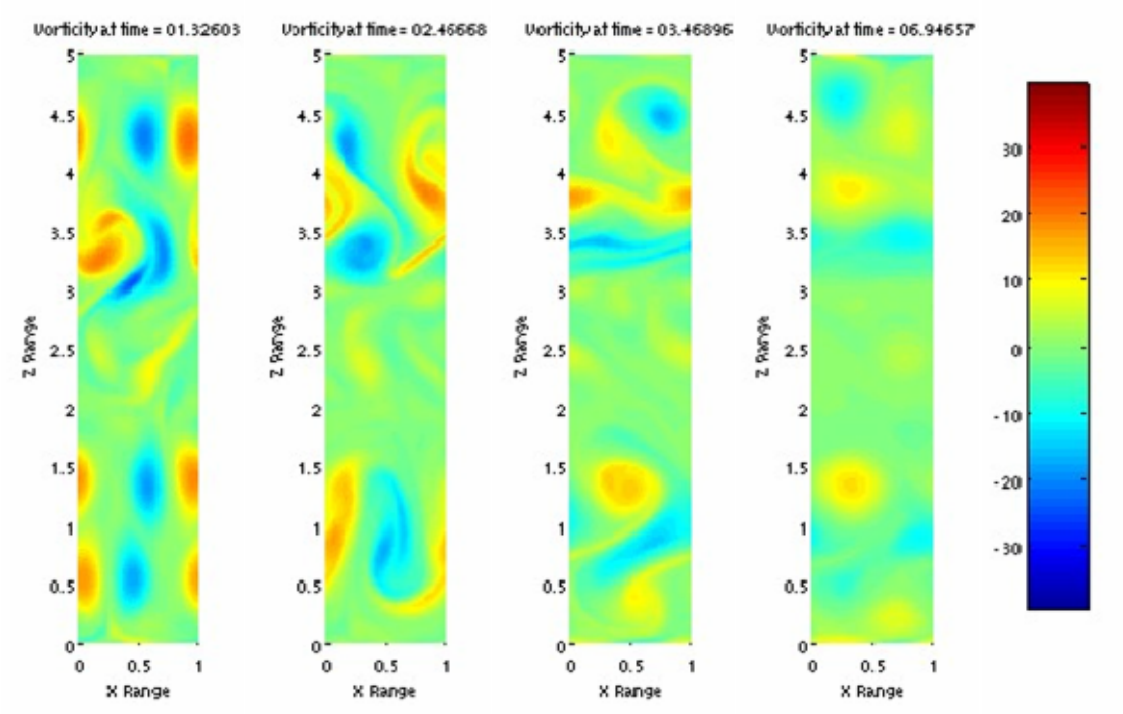

Figure 17. Numerical results for perturbed middle region initial conditions and a exponential density profile with $\alpha = .05$.

3. $\alpha = .1$ in the exponential density profile.

Increasing α further to $\alpha = 0.1$ is displayed in Figure 18. It is seen that the vortices sustain their strength through $t = 1.88430$. As before, there is an initial pairing with the bottom two vortices and then, once again, they split, forming two weaker vortices.

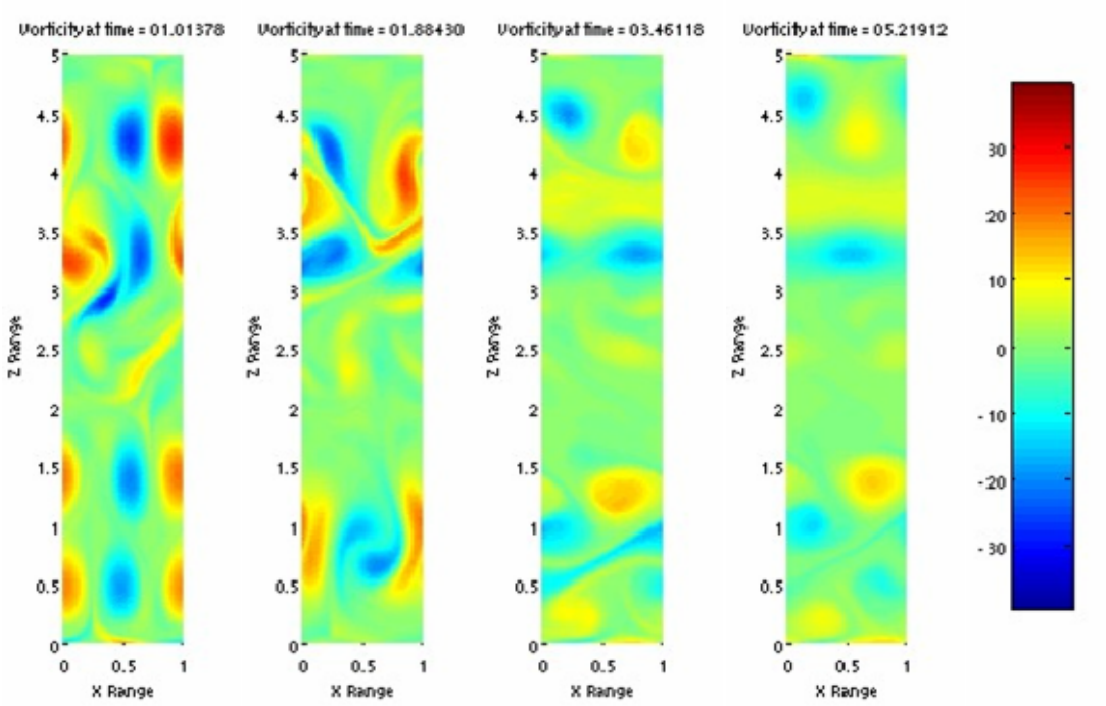

Figure 18. Numerical results for perturbed middle region initial conditions and an exponential density profile with $\alpha = .1$.

b. Hyperbolic Tangent Density Profile

This portion of the analysis observes the development of the structured background density transition layer with the perturbed middle region initial condition using the anelastic equations. Figure 19, below, shows numerical results of this run which is very similar to that shown in Figure 17. It is seen, again, that vortices pair and then diverge over time. In the end, a mixing barrier is formed in the middle of the region that prevents vertical exchanges of fluids.

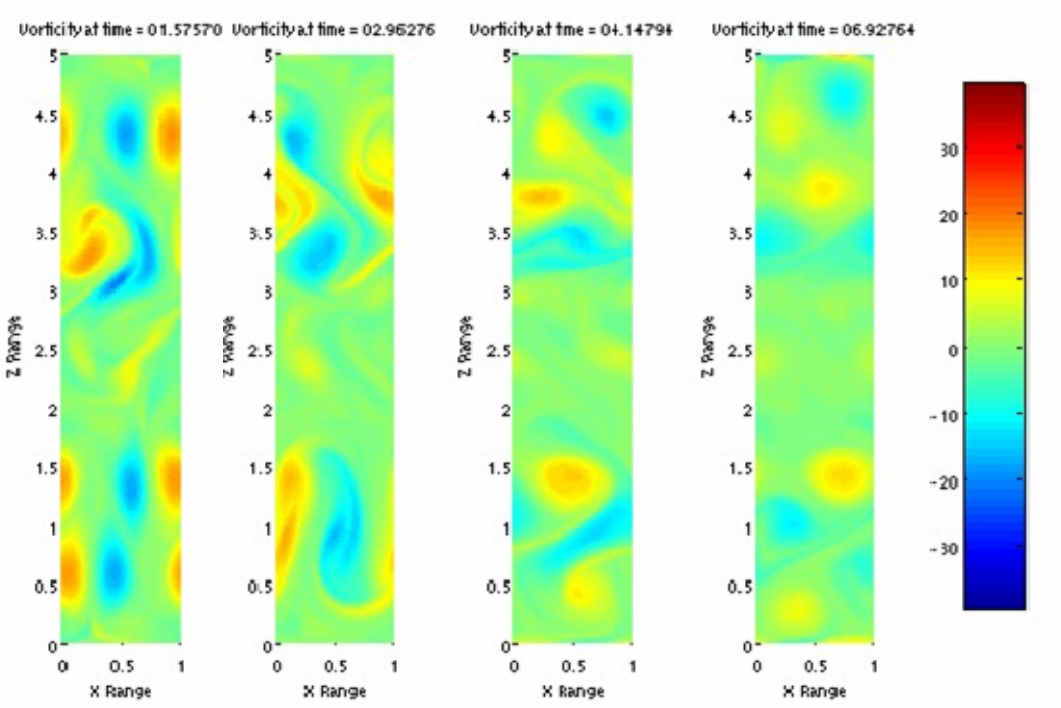

Figure 19. Numerical results for perturbed middle region initial condition with a hyperbolic tangent density profile.

c. Linear Density Profile

Figure 20 shows that there is little variance between this run and the incompressible Navier-Stokes run with the perturbed middle region initial condition, Figure 9. Again, the bottom two vortices merge and then grow apart, becoming weaker. At the final time there is a mixing barrier that restricts the vertical mixing of fluids from the top to bottom and vice versa.

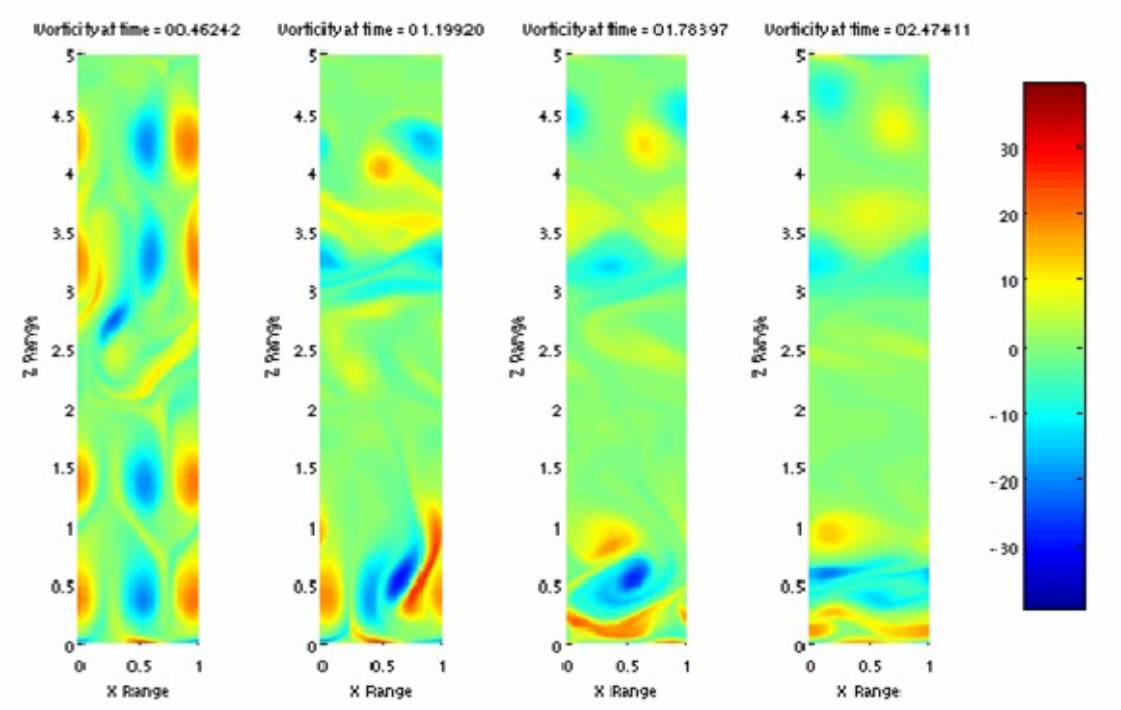

Figure 20. Numerical results for perturbed middle region initial condition and a linear density profile.

3. Poiseuille Flow Initial Condition

The Poiseuille flow initial condition for a weakly compressible fluid flow gave the same results as the incompressible Navier-Stokes flow. One would expect this as the only change in the governing equations is the rate at which the flow rate in the horizontal direction decays. The conservation of mass equation is identically satisfied since the only component of flow is in the x direction but depends only upon the variable z and t. The numerical results confirmed expectations in that there was an imperceptible change in flow from the initial conditions.

IV. CONCLUSIONS

This study has presented numerical models that document a remarkable comparison of weakly compressible fluid flow, incompressible fluid flow, under varying initial conditions and density profiles. The anelastic model provides a numerical method to analyze meteorological phenomenon such as mixing barriers, allowing more efficient use of computer resources by allowing larger time steps and eliminating updates of fluid density evaluations in the time marching scheme.

Unlike the incompressible Navier-Stokes equation, the weakly compressible model with a structured background density transition layer, see Figure 3, and a standard cellular flow initial condition provided a mixing barrier, displayed a limiting vertical fluid exchange within the medium and a noticeable downward shift in the fluid flow. The exponential density profile with $\alpha = 0.02$ and a standard cellular flow initial condition created similar results to that of the incompressible Navier-Stokes equation. Outside vortices paired up first and then moved to the middle of the numerical domain to form an eddy, mimicking the incompressible model. However, when $\alpha = 0.05$, the fluid acts more like the analysis for structured background density transition layer. The top vortices paired up while the middle and bottom two paired, to create a mixing barrier. When $\alpha = 0.1$, the results became unreliable. There was a sudden rush downward of the vortices and then they would stay there swirling, exchanging fluid in small circles at the bottom of the medium. It seems that an increasing α will better model a weakly compressible fluid,

but only to a certain point because the difference in density from top to bottom is too great for a weakly compressible study, causing the results to be unreliable. The standard cellular flow initial condition with a linear density profile also gave unreliable result, leaving holes in the data after $t \approx 1.5$.

The perturbed middle region initial condition presented very different results. This initial condition starting the incompressible Navier-Stokes model produced results that showed vortices not mixing, essentially creating mixing barriers throughout the entire medium with a primary one in the middle, limiting the vertical fluid flow in the medium. For every run there seemed to be mixing of the bottom two vortices and then separation, returning to solitary vortices. When run with other density profiles for the weakly compressible model, the results did not differ greatly from that of the incompressible case. As α increased in the exponential density profile, we saw that the vortices would stay stronger (darker) for a longer period of time, but a lack of mixing and a mixing barrier were still formed. The linear density profile displayed tighter vortices in the bottom region than for any other run.

The Poiseuille flow initial condition presented rather simple results. Since there is no vertical velocity, there are only slight changes in the fluid flow throughout all of the results run. Because the density profiles are functions of depth and the vertical velocity at each depth equaled zero, there was minimal change between the incompressible Navier-Stokes and weakly compressible models.

The second order finite difference method of solving these systems of equations can lead to truncation errors. Future work may be performed using alternative numerical techniques to yield higher order results. One such example would be to use a multi-grid method for spatial discretizations with a Runge-Kutta Method for time marching. Such methods can be run with higher order truncation errors than those of this study (which happened to be second order). While a higher order truncation error will enable more accurate results, it will come at a cost of computational complexity.

It is hoped that this contribution to the field of Meteorology & Oceanography may benefit the Undersea Warfare community within the United State Navy and help efforts to better model and understand meteorological and oceanographic phenomenon. This information could lead to the survival of marines, sailors, and soldiers in the future.

THIS PAGE INTENTIONALLY LEFT BLANK

LIST OF REFERENCES

Bannon, P. R. "On the Anelastic Approximation for a Compressible Atmosphere." *J. Atmos. Sci.* 53 (1996): 3618-3627.

Batchelor, G. K. *An Introduction to Fluid Dynamics*. New York: Cambridge University Pres, 1967

Batchelor, G. K. "The Conditions for Dynamical Similarity of Motions of a Frictionless Perfect-Gas Atmosphere." *Q. J. R. Meteorol. Soc.* 79 (1953): 224-235.

Canuto, C., Hussaini, M. Y., Quarteroni, A., and Zang, T. A. *Spectral Methods in Fluid Dynamics*. New York: Springer-Verlag, 1988.

Chorin, A. J. "Numerical Solution of Incompressible Flow Problems." *Studies in Num. Anal.* 2 (1968): 64-71

Chorin, A. J. and Marsden, J. E. *A Mathematical Introduction to Fluid Mechanics*. New York: Springer-Verlag, 1990.

Durran, D. R. "Improving the Anelastic Approximation." *J. Atmos. Sci.* 46 (1989): 1453-1461.

Dutton, J. A. and Fichtl, G. H.. "Approximate Equations of Motion for Gases and Liquids." *J. Atmos. Sci.* 26 (1969): 214-254.

Gough, D. O. "The Anelastic Approximation for Thermal Convection." *J. Atmos Sci.* 26 (1969): 448-456.

Jarvis, G. and McKenzie, D. "Convection in a Compressible Fluid with Infinite Prandtl Number." *J. Fluid Mech.* 96, no. 13 (1980): 515-583.

Lipps, F. and Hemler, R. "A Scale Analysis of Deep Moist Convection and Some Related Numerical Calculations" *J. Atmos Sci.* 39 (1982): 2192-2210.

McLaughlin, R. M. and Forest, M. G. "An Anelastic Scale-Separated Model for Mixing, with Application to Atmospheric Transport Phenomena." *Phys. Fluids* 11, no. 4 (1999): 880-892.

McLaughlin, R. M., Zhou, H., and Forest, M. G. "Computational Study of a Weakly compressible Mixing Barrier in Low Prandtl Number, Strongly Stratified Fluids." ***Phys. of Fluids*** 15, no. 10 (2003): 2872-2885.

Ogura, Y. and Phillips, N. A. "Scale Analysis of Deep and Shallow Convection in the Atmosphere." ***J. Atmos. Sci.*** 19, no. 2 (1962): 173-179.

Wilhelmson, R. and Ogura, Y. "The Pressure Perturbation and the Numerical Modeling of a Cloud." ***J. Atmos. Sci.*** 29 (1972): 12995-1307.

BIBLIOGRAPHY

Almgren, A. S. "A New Look at the Pseudo-Incompressible Solution to Lamb's Problem of Hydrostatic Adjustment." J. *Atmos. Sci.* 57, no. 7 (2000): 995-998.

Charney, J. G. and Ogura, Y. "A Numerical Model of Thermal Convection in the Atmosphere." *Proceedings of the International Symposium on Numerical Weather Prediction*, (1960): 431-451

L.B. Nance, L. B. and Durran, D. R. "A Comparison of the Accuracy of Three Anelastic Systems and the Pseudo-Incompressible System." *J. Atmos. Sci.* 51, no. 24 (1994): 3549-3565.

Lindfield, G. and Penny, J. *Numerical Methods Using MATLAB*. Upper Saddle River, New Jersey: Prentice Hall, 2000.

Majda, A. and Bertozzi, A. *Vorticity and Incompressible Flow*. New York: Cambridge University Press, 1992.

Majda, A. and Sethian, J. "The Derivation and Numerical Solution of Equations for Zero Mach Number Combustion." *Combust. Sci. Technol.* 42 (1985): 185205.

Thomas, J. W.. *Numerical Partial Differential Equations: Finite Difference Methods*. New York: Springer, 1995.

THIS PAGE INTENTIONALLY LEFT BLANK

INITIAL DISTRIBUTION LIST

1. Defense Technical Information Center
   Ft. Belvoir, Virginia

2. Dudley Knox Library
   Naval Postgraduate School
   Monterey, California

3. Carlos Borges, Ph.D.
   Department of Applied Mathematics, NPS
   Monterey, California

4. Hong Zhou, Ph.D.
   Department of Applied Mathematics, NPS
   Monterey, California

5. Clyde Scandrett, Ph.D.
   Department of Applied Mathematics, NPS
   Monterey, California